Cytoplasmic mRNA decay by the anti-viral nuclease RNase L promotes transcriptional repression

Xiaowen Mao[1], Sherzod Tokamov[1], Felix Pahmeier[2], Azra Lari[1], Jinyi Xu[3], Eva Harris[2], Britt Glaunsinger[1,3,4*]

[1] Department of Plant and Microbial Biology, UC Berkeley, Berkeley, CA, USA

[2] Division of Infectious Diseases and Vaccinology, School of Public Health, University of California, Berkeley, Berkeley, CA, USA

[3] Department of Molecular and Cell Biology, UC Berkeley, Berkeley, CA, USA

[4] Howard Hughes Medical Institute, UC Berkeley, CA, USA

*To whom correspondence may be addressed. Email: glaunsinger@berkeley.edu

SUMMARY

Ribonuclease (RNase) L is an antiviral factor that promiscuously degrades viral and cellular RNA in the cytoplasm. This causes extensive translational reprogramming and alters mRNA processing and export. Here, we reveal that another major consequence of cytoplasmic RNase L activity is the repression of nascent RNA synthesis in the nucleus. This is not associated with altered nuclear RNA stability but instead results from a global loss of RNA polymerase II (Pol II) occupancy across the genome. Prominent among the transcriptionally downregulated loci are immune-related genes, supporting a role for RNase L in tempering innate immune and inflammatory responses. These transcriptional changes are associated with reduced levels and altered localization of a portion of serine 5-phosphorylated Pol II into nuclear speckles. Crosstalk between RNA decay and transcription thereby contributes to the large-scale modulation of gene expression in RNase L-activated cells.

Introduction

Ribonuclease (RNase) L is an important player in the innate immune response stimulated by double-stranded RNA (dsRNA), a pathogen-associated molecular pattern (PAMP) that is commonly associated with viral infection. RNase L dimerizes and is activated by 2'-5'-oligo(A), a second messenger produced by the oligoadenylate synthetases (OAS) 1-3 upon dsRNA binding. Once activated, RNase L promiscuously cleaves cytoplasmic RNA, including viral RNAs and host rRNA, mRNA, and tRNA, at sites defined by UN^N (Karasik and Guydosh, 2024).

RNase L was initially hypothesized to suppress translation through its ability to cleave rRNA and tRNA. However, rRNA and tRNA cleavage occurs after translation remodeling, and ribosomes with RNase L-cleaved rRNAs can still support translation (Burke et al., 2019; Donovan et al., 2017; Rath et al., 2019). Thus, widespread cleavage of mRNA most likely causes the prominent decrease in cellular translation (Burke et al., 2019; Chitrakar et al., 2019; Rath et al., 2019).

In addition to suppressing viral gene expression, RNase L-induced gene expression reprogramming can moderate the innate immune response in both positive and negative ways (Burke et al., 2021; Burke et al., 2019; Burke et al., 2022; Chitrakar et al., 2019; Karasik et al., 2024; Lee et al., 2023; Malathi et al., 2007; Rath et al., 2019; Xi et al., 2024; Yang et al., 2024). RNAse L has been shown to promote virus-induced IFNβ production in mice and in cells where its basal expression is low, but suppress IFNβ production in cells like macrophages with higher basal RNase L and OAS expression, perhaps to promote tissue protection (Banerjee et al., 2014; Malathi et al., 2007). Additionally, loss-of-function mutations in the OAS-RNase L pathway have been linked to autoimmune diseases, including some cases of multisystem inflammatory syndrome in children following SARS-CoV-2 infection (Lee et al., 2023). These observations suggest that RNase L activity may dampen

immune gene expression to prevent overactivation of the innate immune system. However, some mRNAs encoding antiviral factors are at least partially resistant to RNase L and may be preferentially translated due to the liberated translational resources, ensuring the execution of an antiviral response (Burke et al., 2019; Chitrakar et al., 2019; Rath et al., 2019). Much remains to be learned about the contexts governing the complex roles of RNase L in immune regulation.

While RNA cleavage is a prominent phenotype associated with RNase L, several recent findings reveal additional mechanisms contributing to its impact on gene expression. These include inhibiting mRNA export (Burke et al., 2021), altering mRNA processing (Burke et al., 2022), activating ribotoxic stress responses (Iordanov et al., 2000; Karasik et al., 2024; Xi et al., 2024), and activating RIG-I/MDA5-MAVS pathways through the production of small RNA cleavage fragments (Banerjee et al., 2014; Malathi et al., 2007). Each of these phenotypes relies on RNase L catalytic activity, suggesting that they occur in response to the widespread RNA cleavage.

Several oncogenic gamma-herpesviruses also engage broad-acting mRNA-targeting nucleases whose activity, like RNase L, can lead to upstream alterations in mRNA processing and export (Gaglia et al., 2012; Kumar and Glaunsinger, 2010; Kumar et al., 2011; Lee and Glaunsinger, 2009). Notably, viral cleavage of cytoplasmic mRNA also induces large-scale dampening of RNA polymerase II (Pol II) transcription (Abernathy et al., 2015; Gilbertson et al., 2018; Hartenian et al., 2020). Similarly, widespread cytoplasmic mRNA decay by the cellular exonuclease polyribonucleotide nucleotidyltransferase 1 (PNPT1) that is activated during early apoptosis leads to a subsequent Pol II transcriptional repression (Duncan-Lewis et al., 2021; Liu et al., 2018b; Thomas et al., 2015). These findings indicate there is positive feedback between mRNA synthesis and degradation under conditions of accelerated mRNA decay, which we hypothesized might similarly occur in response to RNase L.

Here, we reveal that activated RNase L causes a global repression of nascent RNA synthesis. This includes interferon-stimulated genes and other immune genes, suggesting that its impact on RNA biogenesis may help temper inflammatory responses. The reduction of newly synthesized RNA is not due to accelerated RNA decay in the nucleus but instead is triggered by RNase L-induced RNA degradation in the cytoplasm. This causes a broad reduction in Pol II occupancy across the genome and an associated changes in the abundance and distribution of serine 5-phosphorylated (S5P) RNA polymerase II (Pol II). Thus, transcriptional repression is a major consequence of cytoplasmic RNase L activation and contributes to the reshaping of the gene expression landscape in cells following innate immune stimulation.

Results

RNase L activation broadly reduces the abundance of newly synthesized RNA in the nucleus

Based on observations of positive feedback between RNA decay and synthesis (Abernathy et al., 2015; Duncan-Lewis et al., 2021), we sought to determine how RNase L impacts the abundance of newly synthesized RNA in the nucleus. We first designed an assay to quantify the total pool of newly transcribed RNA in response to RNase L activation. We activated RNase L by transfecting human A549 cells with the double-stranded RNA mimic poly(I:C) for 4 hours, then added the uridine analog ethynyl uridine (EU) for 30 minutes to label nascent transcripts. The EU-containing RNA was coupled to a Cy5 fluorophore by click chemistry and then visualized by flow cytometry or imaging (Figure 1A). We confirmed that the labeled RNA remained largely nuclear during the 30 min pulse (Figure S1A-B), which is important because upon export to the cytoplasm RNA is rapidly degraded by RNase L.

106 We observed a striking reduction in EU incorporation in poly(I:C) treated WT A549 cells
107 compared to control mock-treated cells (Figure 1B, C). In contrast, poly(I:C) treatment of
108 RNase L knock-out (RLKO) A549 cells resulted in only a modest reduction in EU signal (Figure
109 1B, C), suggesting that RNase L is the primary driver of the loss of newly transcribed RNA in
110 the nucleus. Furthermore, nascent RNA depletion was observed in A549 RLKO cells
111 complemented with WT RNase L but not those complemented with a catalytically dead
112 RNase L mutant R667A (Figure 1B, C), indicating that this effect required RNase L catalytic
113 activity. This phenotype was detected as early as 2 hours after poly(I:C) treatment and grew
114 progressively more pronounced over time (Figure S1C). Poly(I:C) transfection also reduced
115 EU signal in immortalized murine bone-marrow-derived macrophages (iBMDM), and this
116 effect was muted upon siRNA-mediated depletion of RNase L (Figure S1D-E). Although
117 RNase L activation can induce caspase-dependent apoptosis (Siddiqui and Malathi, 2012;
118 Yang et al., 2024), the irreversible pan-caspase inhibitor z-VAD(Ome)-FMK did not prevent
119 the loss of EU signal (Figure S1F), indicating that repression of nascent RNA does not require
120 caspase activation.

121

122 Zika virus is a potent activator of RNase L (Watkins and Burke, 2024; Whelan et al., 2019;
123 Whelan et al., 2021), and we therefore tested whether it also depletes nuclear RNA
124 synthesized during a 30 minute EU pulse. Indeed, Zika virus infection at an MOI of 5 for 24h
125 resulted in a significant reduction in EU-labeled RNA in WT A549 cells compared to RLKO
126 cells as visualized by immunofluorescence (Figure 1D-E, S1G). Interestingly, Zika virus
127 infection cause significant decrease in both WT and RLKO cells compared to mock-infected
128 cells, indicating RNase L-independent mechanism of reducing nuclear nascent RNA. These
129 may include effects induced by dsRNA (Figure 1B-C) and Zika virus capsid protein (Slomnicki
130 et al., 2017). Collectively, these data indicate that RNase L-mediated mRNA degradation
131 represses nascent RNA synthesis, both upon dsRNA transfection and viral infection.

132

133 **RNase L reduces both nascent rRNA and pre-mRNA accumulation**

134 EU is incorporated into transcripts by all three classes of RNA polymerases, with RNA
135 polymerase I (Pol I) and Pol II transcripts each accounting for approximately half of the total
136 signal during a short pulse (Berry et al., 2022). Thus, the loss in EU signal caused by RNase L
137 activation is likely due to the reduction of both nascent Pol I and Pol II transcripts. To
138 comprehensively investigate the nascent transcripts affected by RNase L activation, we
139 sequenced the newly transcribed pool of RNA following pulse labeling for 10 min with
140 another uridine analog, 4-thiouridine (4sU). After adding labeled and unlabeled spike-in
141 controls for normalization, the 4sU-incorporated RNA was purified away from the pre-
142 existing pool of RNA by biotinylation of the 4sU and purification over streptavidin beads
143 (Figure 2A). We confirmed successful enrichment of the 4sU-labeled over unlabeled spike in
144 RNA in our sequencing data and confirmed 4sU RNA enrichment by RT-qPCR using samples
145 treated or untreated with 4sU (Figure S2A-B).

146

147 Initial rRNA filtering indicated that the rRNA reads accounted for no more than 56% of the
148 total reads, which is in line with expectations (Radle et al., 2013). After alignment to the rDNA
149 repeat and spike-in normalization, we observed a decrease in 4sU-seq signal coverage on
150 the entire rDNA repeat in WT cells transfected with poly(I:C) (Figure 2B). We then aligned the
151 remaining reads to the hg38 reference genome and performed a metagene analysis on
152 protein-coding genes. In agreement with the EU flow cytometry data, we observed a global
153 decrease in nascent mRNA transcripts in poly(I:C) treated WT cells relative to mock treated
154 WT cells, as well as in WT cells treated with poly(I:C) compared to RLKO cells treated with
155 poly(I:C) (Figure 2C). We also observed a prominent decrease in several Pol III transcribed
156 genes (Figure S2C). Differential gene expression analysis on protein-coding genes and non-
157 coding genes transcribed by all 3 RNA polymerases revealed a widespread decrease on a
158 gene-by-gene basis, with 36.2% of genes significantly downregulated (Figure 2D). Thus,
159 RNase L plays a major role in repressing the accumulation of nascent rRNA, noncoding RNA,
160 and mRNA.

161 Fewer genes were significantly upregulated in an RNase L-dependent manner, and manual
162 inspection of these genes revealed that their apparent upregulation is largely explained by
163 one of two situations. The first category contains genes that are differentially expressed in
164 these cells even in the absence of poly(I:C) treatment, indicating they are the result of minor
165 genetic/epigenetic differences between the parental WT cell line and the clonal RLKO cell
166 line (Figure S2D-E). The second category includes genes whose apparent upregulation is
167 instead the result of read-through transcription from upstream highly expressed genes
168 (Figure S2F).

169

170 Notably, gene ontology analysis of the downregulated genes revealed an enrichment of
171 genes involved in cytoplasmic translation and the immune response (Figure 2E). The
172 translation term is likely due to the reduction in ribosomal protein-encoding mRNAs, which
173 are known targets of RNase L (Andersen et al., 2009), suggesting a coordinated response
174 with rRNA transcription inhibition to reduce ribosome biogenesis (Shore and Albert, 2022).
175 The abundance of immune-related categories suggests that RNase L-induced suppression
176 of nascent RNA contributes to its impact on the immune response. We validated this result
177 by performing RT-qPCR on selected immune transcripts in total RNA samples using intron-
178 exon spanning primer pairs to measure pre-mRNA (Figure 2F). Indeed, ISGs including IFIT1,
179 RSAD2, OAS1, and OASL displayed decreased pre-mRNA levels in WT cells compared to
180 RLKO cells stimulated with poly(I:C). In contrast, IFNL1 has previously been shown to
181 undergo intron retention upon RNase L activation, and we observed this expected increase
182 (and a similar trend for ISG15) in WT relative to RLKO cells.

183

184 We next considered the extent to which the decrease in ISG pre-mRNA was due to a
185 reduction in interferon (IFN) signal amplification versus a cell-autonomous effect, as we
186 observed decreased levels of both nascent IFNB1 and IFNL1. This is also relevant because
187 degradation and/or export inhibition of interferons and other cytokine cytoplasmic mRNA by
188 RNase L should reduce the level of their encoded secreted proteins, thereby dampening

189 their ability to induce ISG expression in neighboring cells via paracrine signaling. To evaluate
190 this for ISGs, we treated cells concurrently with poly(I:C) and brefeldin A (BFA), which
191 collapses Golgi-ER retrograde transport and inhibits protein secretion (Niu et al., 2005). BFA
192 reduced the difference in nascent mRNA levels between WT and RLKO cells for most of the
193 ISGs we tested, including IFIT1, RSAD2, OAS1, and OASL, confirming the impact of RNase L
194 activity on signal amplification of the interferon pathway (Figure 2F). However, the difference
195 between IL1A nascent mRNA levels in WT versus RLKO cells remained upon BFA treatment,
196 suggesting that the repression of nascent RNA can independently influence some immune
197 genes in a cell-autonomous manner.

198

199 **Reduction of nascent RNA is not due to accelerated nuclear RNA degradation**

200 RNase L is primarily described as a cytoplasmic nuclease (Burke et al., 2022; Cusic and
201 Burke, 2024), however even a small amount of active RNase L in the nucleus could lead to
202 rapid depletion of pre-mRNA. To directly test whether RNase L activation increases
203 degradation of nascent RNA in the nucleus, we measured nascent RNA turnover using an EU
204 pulse chase experiment. We transfected cells with poly(I:C) for 1 hour before EU pulse
205 labeling, a time point when EU incorporation is minimally affected by RNase L activation
206 (Figure S1C, S3A). We then chased with excess uridine over a 3h time course and measured
207 the decay of the labeled RNA. Notably, the rate of RNA decay was similar in A549 WT and
208 A549 RLKO cells, indicating that RNase L does not accelerate nascent RNA decay in the
209 nucleus (Figure 3A). We confirmed that the transfection conditions were sufficient to induce
210 RNase L-specific reduction of nascent RNA (Figure S3A-B, see the "pulse last" sample) and
211 that our measurements largely captured nuclear RNA (Figure S3C-D).

212

213 As an orthogonal way of confirming that the cytoplasmic fraction of RNase L is sufficient to
214 reduce nascent RNA in the nucleus, we complemented the RNase L knockout cells with a
215 Halo-tagged version of RNase L fused to a cytoplasmic retention signal (CRS) (Figure 3B)
216 derived from GDOWN1 (amino acid 250-368) (Zhu et al., 2022). This CRS promotes

217 cytoplasmic retention by both CRM1-dependent and -independent mechanisms and is
218 strong enough to retain HaloTag containing a SV40 nuclear localization signal within the
219 cytoplasm (Figure S3E). As expected, both CRS-Halo-RNase L and Halo-RNase L appeared
220 restricted to the cytoplasm (Figure 3C-E). Furthermore, both constructs reduced EU-pulse
221 labeled nascent RNA levels to a similar extent upon poly(I:C) transfection (Figure 3F-I),
222 indicating that cytoplasmic RNase L is sufficient to reduce nascent RNA in the nucleus. In
223 contrast, cells overexpressing CRS-Halo-NLS, a negative control, did not display such a
224 pattern (Figure 3F, I).

225

226 Taken together, these data argue against nuclear RNA decay as a mechanism by which
227 RNase L represses newly synthesized RNA. They instead indicate that its cytoplasmic RNA
228 decay activity indirectly impacts RNA biogenesis in the nucleus.

229

230 **RNase L reduces serine-5-phosphorylated (S5P) Pol II levels in the nucleus**

231 To investigate whether RNase L activity affects the transcriptional machinery, we first
232 monitored the large RPB1 subunit of Pol II by immunofluorescence, which undergoes
233 progressive phosphorylation within the heptad repeats in its C-terminal domain (CTD). We
234 used antibodies recognizing either the RPB1 N-terminus (i.e., all phosphorylation states), the
235 CTD serine 5 phosphorylated (S5P) version associated with transcription initiation, and the
236 CTD serine 2 phosphorylated (S2P) version associated with elongation. We observed a
237 significant RNase L-specific decrease in the abundance of total (NTD) and S5P Pol II, but not
238 S2P Pol II in poly(I:C)-treated cells (Figure 4A-C, S4A).

239

240 Nuclear speckles are hubs for co-transcriptional RNA processing. While they generally do
241 not contain Pol II, transcriptionally inactive Pol II has been reported within speckles when
242 using an antibody that cross-reacts with both S5P and S2P Pol II (Chapman et al., 2007; Xie
243 et al., 2006). Furthermore, inhibition of Pol II initiation by the CDK7 inhibitor THZ1 causes S5P

244 Pol II to accumulate in nuclear speckles (Hoboth et al., 2024). We similarly observed that
245 poly(I:C) treatment caused a specific accumulation of S5P Pol II in puncta that colocalize
246 with the nuclear speckle marker SC35 (Figure 4D-F, S4A). This S5P clustering in nuclear
247 speckles was less pronounced in RNase L-KO cells (Figure 4D-H). Finally, although nuclear
248 speckle size was unchanged (Figure S4B), there was an increase in SC35 intensity in
249 speckles in poly(I:C)-treated WT cells as well as a more rounded speckle morphology (Figure
250 4I-K). Thus, RNase L activation is associated with a reduction both in the total abundance
251 and a partial redistribution of S5P Pol II, as well as morphological changes to nuclear
252 speckles.

253

254 **RNase L represses transcription via genome-wide reduction of Pol II occupancy**

255 To directly measure how RNase L activation influences Pol II occupancy genome-wide, we
256 performed CUT&RUN-sequencing using an antibody to the Pol II S5P CTD (4H8) and applied
257 Greenlist normalization to account for potential global changes in occupancy. The Greenlist
258 method uses constant nonspecific signals in endogenous regions within the human genome
259 for normalization, which better accounts for the technical and experimental variations (de
260 Mello et al., 2024). Pol II occupancy was globally decreased in poly(I:C)-treated WT
261 compared to RLKO cells or untreated cells (Figure 5A). This RNase L-dependent decrease
262 spanned the length of the genes, including the transcript start site (TSS) (Figure 5B) and
263 transcript end site (TES) (Figure 5C). Analyzing subnucleosomal fragments (<120bp) and
264 nucleosomal fragments (>120bp) separately yielded similar results (Figure S5A-B).

265

266 To obtain a detailed landscape of Pol II occupancy on a gene-by-gene basis, we performed
267 differential binding analysis using DiffBind. This revealed a significant reduction in Pol II
268 binding at 87.1% of the TSS from expressed protein-coding genes in poly(I:C)-treated WT
269 cells compared to RLKO cells (Figure 5D). The 7 loci with increased Pol II binding were
270 associated with minor genetic/epigenetic differences and read-through transcription, akin
271 to the upregulation observed in the 4sU-seq data (Figure S5C-D). Differential binding

272 analysis on occupancy at the TES also revealed a similar decrease in Pol II occupancy (Figure
273 5E). The reduction was apparent both at housekeeping genes (Figure 5F) and at immune
274 genes (Figure 5G). Thus, although immune genes are induced in response to poly(I:C)
275 treatment (Figure 5G), RNase L tempers their level of transcriptional induction.

276 Finally, a subset of genes, including the housekeeping gene EEF1A1 (Figure 5H) and the
277 stress-induced gene JUN (Figure 5I), showed a more pronounced reduction of Pol II
278 occupancy at the 3' end compared to the 5' end, suggesting defects in Pol II transition to
279 productive elongation. Collectively, our Pol II occupancy measurements demonstrate that
280 RNase L activation promotes transcriptional repression, fine-tuning the levels of stress-
281 induced and immune genes while globally downregulating most other genes when cells are
282 under threat.

283

284 Discussion

285 RNase L-induced cytoplasmic mRNA degradation extensively remodels the cellular gene
286 expression landscape, influencing how cells respond to viral infection. Though originally
287 thought to mainly inhibit translation, it is now appreciated that RNase L triggers cascading
288 impacts on upstream stages of gene expression, including mRNA processing and export
289 (Burke et al., 2021; Burke et al., 2022). Here, we demonstrate through EU pulse labeling,
290 nascent mRNA sequencing, and Pol II occupancy experiments that cytoplasmic RNase L
291 activity also profoundly impacts RNA synthesis by repressing early stages of transcription,
292 including at immune genes. RNase L-induced transcriptional repression coincides with
293 changes in nuclear speckle morphology like those previously reported in transcriptionally
294 inhibited cells (Hoboth et al., 2024). It also parallels Pol II transcriptional repression
295 phenotypes induced by viral nucleases and cellular nucleases activated during early
296 apoptosis (Abernathy et al., 2015; Duncan-Lewis et al., 2021; Gilbertson et al., 2018;
297 Hartenian et al., 2020), highlighting the breadth of cellular stresses that engage RNA decay-
298 transcription feedback signaling. The combination of these disruptions to the whole cellular

299 gene expression pathway, spanning RNA synthesis through translation and decay, is likely
300 what renders RNase L such a potent modulator of gene regulation.

301

302 Our data indicate that RNase L affects nascent mRNA via transcriptional inhibition. The most
303 prominent phenotype was reduced Pol II gene occupancy, although RNase L activation also
304 caused a modest reduction of total and S5P Pol II abundance in the nucleoplasm and
305 accumulation of S5P Pol II in nuclear speckles. S5P Pol II occupancy decreased at 87.1% of
306 TSS in an RNase L-dependent manner, suggesting that blocking Pol II recruitment and/or
307 initiation underlies much of the transcriptional repression. Some genes, including JUN, had
308 a more pronounced Pol II reduction at their 3' end, which may reflect additional gene-
309 specific effects on elongation, perhaps induced by stress responses.

310

311 Nuclear speckle-associated proteins play roles in co-transcriptional RNA processing, and
312 genes in close proximity to nuclear speckles often have enhanced expression (Khanna et al.,
313 2014) and splicing efficiency (Bhat et al., 2024; Wu et al., 2024). While active Pol II is not
314 generally found within nuclear speckles, certain forms of inactive Pol II accumulate in the
315 nuclear speckles during stress or upon transcription inhibitor treatment (Bregman et al.,
316 1995; Xie et al., 2006). It is therefore possible that in poly(I:C) treated cells, S5P Pol II is
317 inactive and accumulates in nuclear speckles in response to the dramatic loss in genome-
318 associated Pol II.

319

320 The fact that cytoplasmic RNase L promotes transcriptional repression indicates that its
321 mechanism of action is indirect. We envision several non-exclusive possibilities to explain
322 this connection. The first could involve the relocalization of RNA binding proteins (RBPs)
323 from the cytoplasm to the nucleus. More than 20 RBPs shuttle into the nucleus upon their
324 release from mRNA undergoing degradation by herpesviral nucleases (Gilbertson et al.,
325 2018), and several similarly relocalize in RNase L-activated cells (Burke et al., 2022). Nuclear

326 accumulation of these RBPs alters co-transcriptional RNA processing, including promoting
327 mRNA hyperadenylation and nuclear poly(A) RNA accumulation (Burke et al., 2021; Burke et
328 al., 2022; Decker et al., 2022; Lee and Glaunsinger, 2009). It is also associated with
329 transcriptional repression by herpesviral nucleases (Abernathy et al., 2015; Gilbertson et al.,
330 2018; Hartenian et al., 2020), suggesting that Pol II repression could result from aberrant
331 mRNA processing or export. Second, transcriptional repression may be induced by stress
332 signals conveyed by the global disruption of protein translation and the affected translation
333 machinery. This could occur as a consequence of ZAKα-dependent ribotoxic stress
334 responses or other ribosome quality control pathways induced by RNase L (Karasik et al.,
335 2024; Xi et al., 2024). In support of this hypothesis, nascent protein ubiquitinylation in
336 response to disrupted translation during heat shock contributes to transcriptional
337 repression via a mechanism involving p38 signaling (Aprile-Garcia et al., 2019). Third, RNase
338 L-induced translation arrest could result in a loss of proteins involved in global transcription
339 regulation, particularly those with shorter half-lives. Consistent with this possibility,
340 translation inhibition by cycloheximide in mouse embryonic stem cells can lead to depletion
341 of labile euchromatin modifiers like Chd1 and reduced euchromatin marks, reduced Pol II
342 occupancy, and less nascent RNA (Bulut-Karslioglu et al., 2018). Finally, it is possible that
343 RNA fragments generated by RNase L cleavage serve as signaling molecules in the
344 cytoplasm or upon transit into the nucleus (Takenaka et al., 2025).

345

346 A key outcome of transcriptional repression is modulation of immune gene transcription. We
347 find that although ISGs are robustly induced by poly(I:C) transfection independently of
348 RNase L, RNase L activity tempers ISG induction. Many ISGs are downregulated due to
349 reduced IFN signal amplification, which is relevant considering that RNase L activation is not
350 uniform in cultures of cells exposed to dsRNA and thus decreased gene expression by RNase
351 L should influence innate immune signaling in neighboring cells (Burke et al., 2021; Huai et
352 al., 2025; Rath et al., 2019). However, there are immune genes like IL1A whose transcription
353 is directly repressed by the cytoplasmic RNA decay, indicating that RNase L-induced

354 transcriptional repression can have both cell autonomous and paracrine effects. Given the
355 clinical implications of OAS and RNase L mutations in autoimmune diseases including MIS-
356 C (Karasik and Guydosh, 2024; Lee et al., 2023), elucidating how the RNA decay-driven
357 transcription repression shapes the immune landscape — in coordination with other
358 branches of RNase L-driven pathways — should remain a focus of future studies.

359

360 # Figure legends

361 Figure 1. RNase L-mediated mRNA degradation represses nascent RNA accumulation.

362 (A) Diagram showing the experimental setup for nascent RNA measurement. (B) Flow
363 cytometry histograms of A549 WT or RNase L knockout (RLKO) cells with the indicated
364 treatment from one representative biological replicate (of 3 independent biological
365 replicates). (C) Quantification of flow cytometry data from 3 independent biological
366 replicates. Each dot represents the median fluorescence intensity of the sample with the
367 indicated treatment from one biological replicate, normalized to the median fluorescence
368 intensity of mock-transfected RLKO cells. Bars represent mean ± SD. P-values were
369 calculated using a two-sided Welch's *t*-test. (D) Representative immunofluorescence
370 images (max intensity projection, 3 independent biological replicates) of A549 WT or RLKO
371 cells infected with Zika virus (MOI=5) at 24 hpi. Cells were stained with mouse anti-NS3
372 antibody to indicate infected cells, and Hoechst 33342 to mark nuclei. (E) Quantification of
373 nuclear EU signal in 1 representative replicate of 3 independent biological replicates in *(D)*.
374 Each dot represents the mean nuclear EU fluorescence intensity of one individual nucleus.
375 Bars represent mean ± SD. P-value was calculated using Welch's *t* test.

Figure 2. RNase L reduces nascent rRNA and pre-mRNA.

(A) Diagram summarizing the 4sU-seq experiment. (B) IGV tracks showing 4sU-seq coverage at rDNA repeat. Tracks represent the average coverage of 3 independent biological replicates. (C) Metagene analysis of 4sU-seq signal coverage over expressed protein-coding genes (-1kb from TSS to +2.5kb from TES, n=12,713). Lines represent the average coverage of 3 independent biological replicates. (D) Differential expression analysis of 4sU-seq comparing WT cells transfected with poly(I:C) to RLKO cells transfected with poly(I:C). Each gene was graphed with the log2(fold change) value on the y axis and log2 of mean expression level expressed in count per million (CPM) on the x axis. Significantly-up (red) and significantly-down (blue) are defined as adjusted *p*-value < 0.05 and log2(fold change) > 0.585 or < -0.585, respectively. Dashed lines denote log2(fold change) of -0.585, 0, and 0.585. (E) GO-term enrichment analysis of down-regulated genes identified in *(D)*. (F) Pre-mRNA level of immune genes in WT or RLKO cells transfected with poly(I:C), with or without treatment of brefeldin A (BFA). Pre-mRNA level is determined by RT-qPCR using intron-exon spanning primer pairs, normalized to 18S. *, p< 0.05; **, p<0.01; ***, p< 0.001; ns, not significant.

391 Figure 3. Reduction of nascent RNA is not due to accelerated nuclear RNA degradation by
392 RNase L

393 (A) Quantification of EU signal intensity after uridine chase for durations indicated. Each
394 point represents the average of median EU fluorescence intensity from 3 independent
395 biological replicates, normalized to 0h chase. (B) Diagrams of the constructs used. (C)
396 Representative images of the localization of tagged RNase L. The tagged RNase L was
397 visualized by halo tag labeling with JF646 halo dye. A single z plane is shown per construct.
398 (D) Line profile of CRS-Halo-RNase L shown in *(C)*. (E) Line profile of Halo-RNase L shown in
399 *(C)*. (F) Flow cytometry scatter plot of A549 RLKO cells nucleofected with the indicated
400 constructs, with or without poly(I:C) transfection. Data is from 1 representative replicate of
401 3 independent biological replicates. (G-I) Quantification of EU signals in *(F)*. The Halo
402 intensity is gated at locations shown in (F) and separated into 2 populations. Each dot
403 represents the median fluorescence intensity, normalized to the median fluorescence
404 intensity of mock-transfected RLKO cells nucleofected with the constructs indicated. Bars
405 represent mean ± SD. P-values were calculated using a ratio paired *t*-test.

Figure 4. RNase L reduces serine-5-phosphorylated Pol II levels in the nucleus

(A)-(C) Quantification of total Pol II (NTD), S5P, and S2P staining intensity after transfection as indicated for 4.5h, respectively. Each point represents the mean fluorescence intensity of each nucleus. Data is representative of 3 independent biological replicates. Error bars represent mean ± SD. ****, $p<0.0001$ (Welch's t-test). (D) Representative max-intensity-z-projection images of the S5P Pol II and SC35 localization in poly(I:C)-transfected A549 WT or RLKO cells. Data is representative of 3 independent biological replicates. (E) Magnified view of representative nuclei in *(D)*. (F)-(G) Line profile of S5P and SC35 intensity in *(E)*. (H) Quantification of the ratio of mean S5P intensity in nuclear speckles and in nuclei using data in *(D)*. Each point represents the value calculated for each nucleus. Error bars represent mean ± SD. ****, $p<0.0001$ (Welch's t-test). (I) Quantification of coefficient of variation (CV), defined as $CV=\sigma/\mu$, where σ is the standard deviation and μ is the mean intensity. Data is the same as *(D)*. Each point represents the value calculated for each nucleus. Error bars represent mean ± SD. ****, $p<0.0001$ (Welch's t-test). (J)-(K) Quantification of mean SC35 intensity and circularity for each SC35 focus, respectively, using data in *(D)*. Each point represents the value calculated for each SC35 focus. Error bars represent mean ± SD. ****, $p<0.0001$ (Welch's t-test).

424 Figure 5. RNase L activation inhibits transcription by reducing RNA Pol II occupancy.

425 (A) Metagene analysis of Pol II occupancy on expressed protein-coding genes in WT or RLKO
426 cells, either mock transfected or transfected with poly(I:C). Lines represent the average
427 coverage of 3 independent biological replicates. N=12,713. (B) Metagene analysis of Pol II
428 occupancy at -1kb to +1.5kb around transcription start site (TSS) of expressed protein-
429 coding genes. Lines represent the average coverage of 3 independent biological replicates.
430 N=12,713. (C) Metagene analysis of Pol II occupancy at -1kb to +1.5kb around transcript end
431 site (TES) of expressed protein-coding genes. Lines represent the average coverage of 3
432 independent biological replicates. N=12,713. (D) Differential binding analysis of CUT&RUN-
433 seq signal at the TSS (-500bp to +50bp) comparing WT cells transfected with poly(I:C) to
434 RLKO cells transfected with poly(I:C). Each locus was graphed with the log2(fold change)
435 value on the y axis and the mean expression level on the x axis. Significantly-up (red) and
436 significantly-down (blue) are defined as adjusted *p*-value < 0.05 and log2(fold change) >
437 0.585 or < -0.585, respectively. Dashed lines denote log2(fold change) of -0.585, 0, and 0.585.
438 (E) Differential binding analysis of CUT&RUN-seq signal at the TES (-100bp to +500bp)
439 comparing WT cells transfected with poly(I:C) to RLKO cells transfected with poly(I:C).
440 Significantly-up (red) and significantly-down (blue) are defined as adjusted *p*-value < 0.05
441 and log2(fold change) > 0.585 or < -0.585, respectively. Dashed lines denote log2(fold
442 change) of -0.585, 0, and 0.585. (F) IGV tracks showing Pol II CUT&RUN signal coverage on
443 HSPA8 and RPL13, two examples of housekeeping genes. (G) IGV tracks showing Pol II
444 CUT&RUN signal coverage on IFNL1 and B2M, examples of immune genes. (H)-(I) IGV track
445 overlay showing Pol II CUT&RUN signal coverage on EEF1A1 and JUN genes. All tracks in *(F)-*
446 *(I)* represent the average coverage of 3 independent biological replicates.

447 Figure S1. RNase L activation reduces nascent RNA progressively in A549 and iBMDM cells,
448 independent of caspase activity. Related to Figure 1

449 (A) Representative max-intensity-projected images of mock-transfected A549 WT cells
450 pulsed with 1mM EU for 30 minutes. (B) Normalized fluorescence intensity across line trace
451 in (*A*). (C) A549 WT or RLKO cells were either mock-transfected with RNAiMAX or transfected
452 with 0.76μg/ml poly(I:C) for durations indicated, followed by a 30-min pulse labeling with 1
453 mM EU. Error bars represent the mean ± SD of log2-fold change over mock-transfected
454 RNase L KO cells at the indicated time point. Data is from 2 biological replicates. (D) Murine
455 iBMDM cells were nucleofected with either control or RNaseL-targeting siRNA for 48 hours,
456 either mock-transfected with RNAiMAX or transfected with 0.76μg/ml poly(I:C) for 4 hours,
457 followed by a 30-minute pulse labeling with 1 mM EU. EU signal was gated according to no-
458 EU controls. Error bars represent mean ± SD of 3 biological replicates. (E) Western blot
459 validation of RNase L siRNA knockdown efficiency. (F) A549 WT or RNase L KO cells were
460 transfected with 0.76μg/ml poly(I:C) in the presence of z-VAD at the indicated concentration
461 for 4 hours, followed by 30-min pulse labeling with 1mM EU. Each dot represents the median
462 fluorescence intensity of the sample with indicated treatment from one biological replicate,
463 normalized to the median fluorescence intensity of DMSO-treated KO cells. Bars represent
464 mean ± SD. P-values were calculated using a two-sided Welch's *t*-test. Data is from 2
465 biological replicates. (G) Low magnification (20X) field of view of Zika virus-infected cells,
466 from the same sample as *Figure 1D-E*.

467 ?

468 Figure S2. 4sU-seq data accurately captures changes on the nascent RNA level. Related to
469 Figure 2.

470 (A) Differential expression analysis of 4sU-seq comparing WT cells to RLKO cells transfected
471 with poly(I:C) cells (same as Figure 2D), with spike-ins highlighted. See Figure 2D for details.
472 (B) RT-qPCR of 4sU samples compared to no-4sU control. RNA samples were the same as
473 the ones used in 4sU-seq. *, $p < 0.05$ (ratio paired *t* test). (C) IGV tracks showing 4sU-seq
474 signal coverage on RN7SK, VTRNA1-3 and RN7SL3, examples of downregulated Pol III
475 transcribed genes. Tracks represent the average coverage of 3 independent biological
476 replicates. Positive value indicates coverage in the positive strand direction while negative
477 value indicates coverage in the negative strand direction. (D) Differential expression analysis
478 of 4sU-seq comparing mock-transfected WT cells RLKO cells. (E) IGV tracks showing 4sU-
479 seq signal coverage on CADM2, an example of cell line-specific expression variation. Tracks
480 represent the average coverage of 3 independent biological replicates. Positive value
481 indicates coverage in the positive strand direction while negative value indicates coverage in
482 the negative strand direction. (F) IGV tracks showing 4sU-seq signal coverage on FAP
483 downstream of IFIH1, an example of read-through transcription. Tracks represent the
484 average coverage of 3 independent biological replicates. Positive value indicates coverage in
485 the positive strand direction while negative value indicates coverage in the negative strand
486 direction.

487 Figure S3. EU pulse chase experiments accurately measure nuclear RNA turnover kinetics
488 and functional confirmation of the CRS tag. Related to Figure 3.

489 (A) Diagram showing the experimental setup of the "EU pulse last" control in parallel to the
490 EU pulse chase experiments shown in Figure 3A. (B) Quantification of EU signal in the "EU
491 pulse at last" control. Data from Figure 3B, replotted as the ratio of EU signals in A549 WT to
492 RLKO cells, are included for comparison. Each dot represents one biological replicate. Bars
493 represent mean ± SD. (C) Representative max-intensity-projected images of cells
494 transfected with poly(I:C) for 1 hour, pulsed with 1mM EU for 30 minutes then chased for 2
495 hours. WT cells were labeled with CFDA-SE dye and co-cultured with RLKO cells. (D)
496 Normalized fluorescence intensity across line trace in *(C)*. CFDA-SE signal is included as a
497 uniform distributed control for comparison. (E) Representative images of the localization of
498 CRS-Halo-NLS and Halo-NLS. A single z plane is shown per construct. Diagram showing the
499 constructs are included.

500 Figure S4. RNase L activation reduces nuclear total Rpb1 and S5P Rpb1 and does not affect
501 nuclear speckle sizes. Related to Figure 4.

502 (A) Representative max-intensity-z-projection images of Pol II (NTD), S5P and S2P staining in
503 A549 WT or RLKO cells transfected as indicated. Data are the same as Figure 4A-C. (B)
504 Quantification of SC35 foci area for each SC35 focus using data in Figure 4D. Each point
505 represents the value measured for each SC35 focus. Error bars represent mean ± SD. Data
506 are from 1 representative replicate of 3 total replicates.

507

508

509 Figure S5. RNase L activation reduces CUT&RUN subnucleosomal and nucleosomal signals
510 at TSS, and CUT&RUN-seq mirrors apparent upregulation in 4sU-seq. Related to Figure 5.

511 (A) Metagene analysis of subnucleosomal fragment (<120bp) coverage at -1kb to +1.5kb
512 around transcription start site (TSS) of expressed protein-coding genes. (B) Metagene
513 analysis of nucleosomal fragment (>120bp) coverage at -1kb to +1.5kb around the
514 transcription start site (TSS) of expressed protein-coding genes. The enrichment of
515 subnucleosomal fragments slightly upstream of TSS and the bimodal peaks around the TSS
516 of the nucleosomal fragments likely reflect the local nucleosome organization around Pol II
517 occupancy sites. (C) IGV tracks showing Pol II CUT&RUN-seq and 4sU-seq signal coverage
518 on ZNF724, an example of cell line-specific expression variation. Tracks represent the
519 average coverage of 3 independent biological replicates. For the 4sU track, positive value
520 indicates coverage in the positive strand direction while negative value indicates coverage in
521 the negative strand direction. (G) IGV tracks showing Pol II CUT&RUN-seq and 4sU-seq signal
522 coverage on GALR3 downstream of H1-0, an example of read-through transcription. Tracks
523 represent the average coverage of 3 independent biological replicates. For the 4sU track,
524 positive value indicates coverage in the positive strand direction while negative value
525 indicates coverage in the negative strand direction.

526 # Materials and Methods

527 **Plasmids**

528 All plasmids generated in this study were sequence verified by whole plasmid sequencing
529 and have been deposited on Addgene (accession numbers pending). All PCR reactions were
530 performed using Q5 2X master mix (NEB, cat # M0494S). Sequences encoding the CRS tag,
531 HALO tag, and RNase L with appropriate overhangs were PCR amplified. pLJM1-Halo-
532 RNaseL was constructed by directly cloning the HALO and RNase L PCR fragments into
533 linearized pLJM1-puro (Sancak et al., 2008) using InFusion (Takara Bio, Cat # 639650). pLJM1-
534 CRS-Halo-RNaseL was constructed by first assembling CRS, HALO and RNase L PCR
535 fragments into a single fragment by overlap extension PCR, followed by cloning into
536 linearized pLJM1-puro using InFusion. pLJM1-CRS-Halo-NLS was generated from pLJM1-
537 CRS-Halo-RNaseL using a site-directed mutagenesis protocol described previously (Chiu et
538 al., 2004) to replace RNase L fragment with an SV40 NLS (PKKKRKV). pLJM1-Halo-NLS was
539 generated from pLJM1-Halo-RNaseL using the same mutagenesis method as above.

540

541 **Cells and culture conditions**

542 A549 WT, RLKO, RLKO-RL and RLKO-CM cell lines were generously provided by James Burke
543 (University of Florida Scripps) and Roy Parker (University of Colorado, Boulder). Immortalized
544 murine bone marrow macrophages were generously provided by Susan Carpenter (UC Santa
545 Cruz). All cell lines were maintained in DMEM supplemented with 10% FBS and tested for
546 mycoplasma routinely using Universal Mycoplasma Detection Kit (ATCC, cat # 50189644FP).

547

548 **EU pulse chase for flow cytometry**

549 Cells were were mock-transfected or transfected with 0.76μg/ml poly(I:C) HMW (InVivoGen,
550 cat # tlrl-pic) using Lipofectamine RNAiMAX (Thermo Fisher, cat # 13778-150) as indicated,
551 then the media was replaced with 1mM EU (Click Chemistry Tools cat #CCT-1261-500 or

552 Lumiprobe cat # 2439-500mg) in DMEM with 10% FBS. The cells were incubated at 37°C for
553 30 minutes. For flow cytometry samples, cells were washed once with 1ml PBS, harvested,
554 and fixed with 1% PFA. The cells were then permeabilized by resuspending in 100ul 0.05%
555 w/v saponin in PBS. To visualize EU incorporation, 500ul click reaction mix (4mM $CuSO_4$,
556 100mM sodium ascorbate, 2 μM sulfo-cyanine5-azide (Lumiprobe cat# A3330) in TBS,
557 50mM Tris-HCl, pH 8.0, 150mM NaCl) was added to the cell suspension and the samples
558 were incubated at room temperature for 30 minutes, protected from light. The samples were
559 then washed twice with 1ml 0.05% w/v saponin in PBS, once with 1ml PBS, then
560 resuspended in PBS before flow cytometry analysis. The samples were then analyzed on an
561 BD Accuri C6 Plus flow cytometer.

562 For EU pulse chase experiments, WT cells were first color-labeled with 1 μM CFDA-SE
563 (cayman chemical, cat # 14456) in PBS for 10 min at room temperature, quenched with equal
564 volume of DMEM with 10% FBS, then washed with DMEM with 10% FBS 3 times. The labeled
565 WT cells were resuspended in DMEM with 10% FBS, pooled with unlabeled RLKO cells at a
566 1:1 ratio and were seeded in 6-well plates the day before experiment. Cells were transfected
567 with 0.76μg/ml poly(I:C) HMW (InVivoGen, cat # tlrl-pic) using Lipofectamine RNAiMAX
568 (Thermo Fisher, cat # 13778-150) for 1 hour and pulsed with 1mM EU in DMEM with 10% FBS
569 for 30 minutes at 37°C. The EU-containing media was removed, and cells were washed with
570 PBS once and immediately chased with 10mM uridine in DMEM with 10% FBS. The samples
571 were harvested at the indicated time-points. An additional well without transfection and EU
572 pulse labeling was harvested at the same time as the 0-hour chase samples, serving as a
573 no-EU control. The "Pulse last" sample, which served as a control for transfection efficiency,
574 was transfected with 0.76μg/ml poly(I:C) for 1 hour, incubated DMEM with 10% FBS without
575 EU for 30 minutes at 37°C, washed with PBS once and replaced the supernatant with DMEM
576 with 10% FBS and incubated for 1.5 hours. Then the cells were pulsed with 1mM EU in DMEM
577 with 10% FBS for 30 minutes at 37°C and harvested at the same time as the 2-hour chase
578 samples.

579 To characterize EU incorporation in cells overexpressing tagged RNase L, A549 RLKO cells
580 were first nucleofected with the indicated construct using Neon transfection system

581 (Invitrogen) according to the manufacturer's recommended settings for A549 cells (1230V,
582 30ms, 2 pulses), using 5µg DNA per 750,000 cells in 100µL E2 buffer. The nucleofected cells
583 were cultured in 6-well plates overnight. The cells were then incubated with 20nM Halo
584 ligand Janelia Fluor 646 (Promega, cat # GA1121) diluted in 1mL DMEM + 10%FBS per well
585 30 minutes prior to poly(I:C) transfection, then transfected with 0.76µg/ml poly(I:C) for 4
586 hours without removing the Halo dye and pulsed with 1mM EU for 30 minutes same as above.
587 The samples were processed as above, with the exception that 5uM Alexa Fluor™ 488 Azide
588 (Thermo Fisher, cat #A10266) was used.

589

590 To characterize EU incorporation in murine iBMDM cells depleted of RNase L, cells were
591 maintained in DMEM with 10% FBS and grown to 90% confluence. Cells were removed and
592 washed once with Dulbecco's phosphate-buffered saline (DPBS) (Gibco). Nucleofections
593 were done using the Neon Transfection System (Thermo Fisher). 2×10^6 cells were
594 resuspended in 100 µL of buffer R, to which control non-targeting or RNase L targeting pools
595 of siRNA (ON-TARGETplus SMARTpool siRNA – Horizon Discovery) were added to a final
596 concentration of 200nM. This was loaded into a Neon 100-µL pipette tip and Neon tube with
597 3 mL of buffer E2 with electroporation parameters set to 1,680 V, 20 ms, 1 pulse. Following
598 electroporation, cells were plated in 10 mL of DMEM with 10% FBS in 10 cm TC-treated
599 plates and were incubated at 37°C for 24 hours. Cells were then transfected with 0.76µg/ml
600 poly(I:C) pulsed with 1mM EU for 30 minutes same as above. The samples were processed
601 as above.

602

603 **Immunofluorescence**

604 For Zika infection in Figure 1D-E and Figure S1G, A549 WT or RLKO cells were seeded in glass-
605 bottomed 24 well-plates at a density of 100,000 cells per well the day before experiment,
606 and after media change were infected with Zika virus (Nica 2–16, GenBank accession
607 KX421194.1) at an MOI = 5 for 24 hours. Cells were treated with 1 mM EU for 30 min before
608 they were washed once with 1ml PBS then fixed with 4% PFA for 15 minutes. The cells were

609 then permeabilized with 0.5% Triton X-100 in PBS for 15 minutes and washed 3 times with
610 PBS. Samples were then incubated with 500μL click reaction mix at room temperature for 30
611 minutes, then washed twice with PBS and kept in PBS. Samples were then blocked with 1%
612 BSA in PBS with 0.02% Tween-20 for 1 hour and incubated with mouse anti-NS3 antibody
613 (Clone E1D8) (Balsitis et al., 2009) diluted 1:100 in the blocking solution overnight at 4°C.
614 The samples were then washed 3 times with PBS+0.02% Tween-20, incubated with goat anti-
615 mouse IgG AlexaFluor Plus 488 (Invitrogen, cat #A32723) diluted 1:1000 in blocking solution,
616 and washed 3 times with PBS+0.02% Tween-20. The nuclei were stained with 8 μM Hoechst
617 33342 in PBS for 30 minutes, followed by 2 PBS washes.

618 For RNase L localization studies, A549 RLKO cells were nucleofected as in the "EU pulse
619 chase for flow cytometry" section and 340,000 cells were seeded per well in a glass-
620 bottomed 24-well plate and incubated overnight. Cells were first labeled with 20nM Halo
621 ligand Janelia Fluor 646 for 30 minutes and transfected with poly(I:C) at a concentration of
622 0.76μg/ml for 4 hours without removing the Halo ligand. The cells were then pulse labeled
623 with EU and fixed, permeabilized, labeled with click reaction and Hoechst 33342 as above.

624 For characterizing changes in RPB1 and nuclear speckle morphology, A549 WT or RLKO cells
625 were seeded in glass-bottomed 24 well-plates at a density of 100,000 cells per well the day
626 before experiment and transfected with either lipofectamine RNAiMAX alone or with poly(I:C)
627 at a concentration of 0.76μg/ml for 4 (optionally pulsed with 1mM EU for 30min) to 4.5 hours.
628 Samples fixed and permeabilized and optionally labeled with click reaction as above, then
629 were blocked with 0.3%-0.5% BSA in PBS with 0.3-0.5% Triton X-100 for 0.5-1 hour. Then
630 samples were stained with primary antibodies against Rpb1 NTD (clone D8L4Y, Cell
631 Signaling Technology, 1:500), Rpb1 S5P (ab5131, Abcam, 1:500), Rpb1 S2P (ab5095, Abcam,
632 1:500) and SC35 (ab11826, Abcam, 1:500) diluted in blocking solution overnight at 4°C, goat
633 anti-rabbit IgG AlexaFluor Plus 488 (Invitrogen, cat #A32723) alone or goat anti-mouse IgG
634 AlexaFluor 546 (Invitrogen, cat # A11035) and goat anti-rabbit IgG AlexaFluor 647 (Invitrogen,
635 cat # A27040) diluted 1:1000 in blocking solution as secondaries, and 8-10μM Hoechst
636 33342.

All samples were imaged on a Nikon Eclipse Ti spinning disk confocal microscope or a Zeiss LSM 880 confocal laser scanning microscope.

Image processing

All confocal image processing was performed using FIJI, either manually or with custom macros. Line profile measurements were performed using the plot profile function and the data was exported to Prism 10 for normalization and visualization. For nuclear signal quantification in Figure 1D-E and Figure 4A-C, the nuclear regions of interest (ROIs) were generated from the Hoechst channel in the image z-stack by Gaussian blur, thresholding with the Otsu method, and 3D segmentation using the 3D Manager. To fill holes within ROIs and exclude objects on edges, the 3D segmentation map was converted to binary, followed by “3D fill holes” and “3D exclude edges”. The processed binary map was 3D segmented again using the 3D Manager to generate the final ROIs. The ROIs were then used to quantify mean intensity in selected channels with the “quantify” function in 3D Manager.

For quantification in Figure 4I, the image z-stack was first max-intensity projected. Then the nuclear ROIs were generated from the Hoechst channel by Gaussian blur, thresholding with the Otsu method, hole filling by the “Fill holes” function, and size selected with the “Analyze particle” function to only include particles larger than 50 μm^2. Then the ROIs were used to quantify mean intensity and standard deviation in selected channels with the “Measure” function. For analysis in Figure 4H, a 0-and-1-based binary mask for the nuclear speckles was first generated from the SC35 channel by Gaussian blur and local thresholding with the Bernsen method. The mask was multiplied with the S5P channel to isolate S5P signal in nuclear speckles. The measurement for the total nuclear S5P or nuclear speckle S5P signal in nuclei was carried out as above. For nuclear speckle analysis, a 0-and-1-based binary mask for the nuclei was first generated, then the channels of interest were multiplied to the mask to isolate nuclei. A duplicated SC35 channel was then used to generate nuclear speckle ROIs by Gaussian blur, local thresholding with the Bernsen method, size selected with the “Analyze particle” function to only include particles larger than 0.4 μm^2. Then the

665 ROIs were used to quantify mean intensity, area, and circularity in original SC35 channel with
666 the "Measure" function.

667

668 **4sU-Seq**

669 Six million A549 WT or RLKO cells were seeded in 15cm tissue culture dishes and cultured
670 overnight before transfection. Then cells were then transfected with poly(I:C) for 4 hours,
671 followed by pulse labeling with 500μM 4sU dissolved in DMEM media supplemented with 10%
672 FBS for 10 minutes. The plates were washed once with PBS then lysed with 2ml TRIzol. RNA
673 was extracted from the TRIzol lysate, followed by isopropanol precipitation. 100μg or 300μg
674 (WT with poly(I:C)) total RNA was biotinylated with HPDP-biotin (Thermo Scientific cat #
675 PI21341, 50μg per 25μg of RNA) for 2 hours, followed by two chloroform extraction and
676 isopropanol precipitation. The RNA samples were denatured at 65°C for 5 minutes, then
677 incubated with Dynabeads MyOne Streptavidin C1 magnetic beads (Thermo Fisher cat #
678 65002) previously blocked with glycogen for 1 hour. The beads were washed twice with wash
679 buffer (100 mM Tris-HCl, 10 mM EDTA, 1 M sodium chloride, and 0.1% Tween 20) at 65°C
680 then twice at room temperature. To increase the stringency of the washes, the beads were
681 further washed with TE buffer (10mM Tris-HCl pH 7.4, 1mM EDTA) twice at 55°C (Li et al.,
682 2017). 4sU-RNA was then eluted from beads twice with 100μL 100mM DTT, and the
683 combined eluent was precipitated with isopropanol.

684 The sequencing library was constructed using KAPA Stranded RNA-Seq Kit with RiboErase
685 (HMR) (cat # KK8484, 07962304001) following manufacturer's instructions, with the
686 following modifications: Briefly, 60ng to 100ng RNA was used as input without rRNA
687 depletion and fragmented at 85 °C for 6 minutes; the PCR cycle numbers were determined
688 empirically by qPCR. The library was submitted to QB3-Berkeley Genomics Sequencing Core
689 for QC and sequencing on a NovaSeq 6000 S1 chip.

690

691 **Analysis of published RNA-seq datasets**

692 Published total RNA-seq datasets for mock- or poly(I:C)-transfected A549 cells (GEO:
693 GSE124144) (Burke et al., 2019) were used to as a proxy to assign the dominant transcript
694 for each gene. The raw fastq files were first pre-processed using HTStream
695 (https://github.com/s4hts/HTStream) then pseudo-aligned and quantified using Kallisto
696 (Bray et al., 2016). For each gene, the highest expressed transcript (measured by transcript-
697 per-million, TPM, first criteria) with the longest transcript length (second criteria) was
698 selected as the dominant transcript. Only genes on the main nuclear chromosomes (i.e.,
699 chr1-22, chrX and chrY) and the corresponding dominant transcript with average TPM > 0 are
700 included.

701

702 **4sU-Seq data processing**

703 The raw reads were pre-processed with HTStream v1.3.2
704 (https://github.com/s4hts/HTStream), including separation of rRNA and non-rRNA reads
705 into separate files by HTStream SeqScreener. The rRNA reads were aligned to the rDNA
706 repeat (GenBank Accession U13369.1) concatenated with ERCC sequences and the non-
707 rRNA reads were aligned to the human genome (hg38) concatenated with ERCC sequences
708 using STAR v2.6.1b (Dobin et al., 2013). When aligning rRNA reads, options *--alignIntronMax*
709 *1* and *--alignSJDBoverhangMin 999* were set to suppress gapped alignment. Aligned reads
710 were counted using Rsubread (v2.16.1) FeatureCounts (Liao et al., 2014) and differential
711 gene expression analysis was performed with limma-Voom v3.58.1, normalized to 4sU-
712 labeled spike-in. (Ritchie et al., 2015). A model of ~0+group+replicate is used to account for
713 batch effects. Segments of pre-rRNA (i.e., 5' ETS, 18S, ITS1, 5.8S, ITS2, 28S, 3' ETS) were
714 included in the differential expression analysis. Scaled, stranded BigWig files were
715 generated with Deeptools bamCoverage function, using scaling factors generated in limma-
716 Voom (proportional to the reciprocal of norm.factors × lib.sizes). BigWig files of biological
717 replicates were averaged using Deeptools bigwigAverage function. For both operations, bin
718 sizes were set to 20bp. The metagene coverage plots were generated using Deeptools

719 (Ramirez et al., 2016) using the coordinates of dominant transcripts defined in "Analysis of
720 published RNA-seq datasets".

721

722 **CUT&RUN-sequencing**

723 CUT&RUN was done according to previous reports (Miura and Chen, 2020; Morgens et al.,
724 2025) with modifications. Briefly, 250,000 A549 WT or RNase L KO cells per well were seeded
725 on a 12-well plate and cultured overnight before transfection. Then cells were then
726 transfected with RNAiMAX alone or with 0.76 μg/ml poly(I:C) for 4 hours The cells were
727 permeabilize on plate with 500μL Perm buffer (20 mM HEPES-KOH pH 7.5, 150 mM NaCl, 0.5
728 mM Spermidine (Sigma, S2626), 0.1% Triton X-100 (Sigma, X100), and proteinase inhibitor
729 (Roche, 04693132001)) for 15 minutes at room temperature. The cells were washed again
730 with Perm buffer then incubated with either anti-Rpb1 S5P CTD (4H8, Cell Signaling, cat
731 #2629) at 1:50 dilution in 200μL Perm buffer or equal mass of mouse normal IgG (Santa Cruz,
732 cat # sc-2025) for 1 hour at room temperature. The cells were then washed twice with Perm
733 buffer and incubated with pAG-MNase (Cell Signaling, cat #40366) at 1:33 dilution in 200μL
734 Perm buffer for 1 hour at room temperature. The cells were then washed twice with Perm
735 buffer and chill on ice. Then 225 μL ice-cold Perm buffer containing 5 mM $CaCl_2$ was
736 dispensed per well, and the plate was incubated in a refrigerator at 4°C for 30 min for
737 targeted digestion. The reaction was halted by adding 75 μL 4× STOP solution (680 mM NaCl,
738 40 mM EDTA, 8 mM EGTA, 100 μg/ml RNase A (Invitrogen, cat # 12091021) and 0.1% Triton
739 X-100, spiked with yeast genomic DNA (Cell Signaling, cat #40366) at 10pg per sample). The
740 plate was then incubated at 37°C for 30min to facilitate fragment release. The supernatant
741 was collected and then 3μL 20% SDS solution and 3.75μL 20mg/ml proteinase K solution
742 was added. The mixture was then incubated at 50°C for 1 hour. The DNA was extracted with
743 phenol:chloroform.

744 The sequencing library was constructed with NEBNext® Ultra™ II DNA Library Prep Kit (NEB,
745 cat # E7645L) following a previous report (Liu et al., 2018a) with modifications. Briefly, equal
746 volume of purified DNA fragments was used. End prep was performed at 20°C for 30 min and

747 then 50°C for 60min to prevent short fragment melting. Fragments were then ligated to
748 adaptors from NEBNext® Multiplex Oligos for Illumina® (Unique Dual Index UMI Adaptors
749 DNA Set 1, NEB, cat # E7395S) and cleaned up twice with 1.1X Ampure XP beads (Beckman
750 Coutler, cat # A63880). The resulting ligated products were then PCR amplified for 10 cycles
751 and 14 cycles for 4H8 and IgG samples, respectively. The cycle numbers were determined
752 empirically by qPCR. The amplified libraries were double-sided size selected with 0.6X and
753 1.1X Ampure XP beads and further cleaned up by 1 round or 3 rounds with 1.1X bead for 4H8
754 or IgG samples, respectively, to remove adaptor dimers. The library was pooled and
755 sequenced on AVITI platform (Element Biosciences) by UC Davis sequencing core.

756 **CUT&RUN data processing**

757 Reads were trimmed with Trimmomatic v0.39 (Bolger et al., 2014) and aligned to a
758 concatenated human (hg38) and yeast (SacCer3) genome with bowtie 2 v2.5.2 (Langmead
759 and Salzberg, 2012). The BAM files were then deduplicated with UMI_tools v1.1.5 (Smith et
760 al., 2017) and optionally splitted into subnucleosomal (<120bp) and nucleosomal (>120bp)
761 fractions using Deeptools (v3.5.5) alignmentSieve. The normalization factors were
762 calculated according to de Mello et al (de Mello et al., 2024), using Deeptools
763 multibamSummary functions to quantify reads in the Greenlist regions provided and to
764 calculate scaling factors. BigWig files were generated with Deeptools bamCoverage function,
765 using scaling factors generated above. BigWig files of biological replicates were averaged
766 using Deeptools bigwigAverage function. For both operations, bin sizes were set to 20bp. The
767 metagene coverage plots were generated using Deeptools. Differential binding analysis was
768 performed with DiffBind v3.12.0 (Ross-Innes et al., 2012) using the reciprocal normalization
769 factors generated above.

770

771 **Quantitative reverse transcription PCR (RT-qPCR)**

772 For Figure 2F, 500,000 A549 WT or RLKO cells per well were seeded in 6-well plates the day
773 before experiment and were either mock-transfected or transfected with 0.76μg/ml poly(I:C),
774 in the absence or in the presence with 1X brefeldin A (eBiosciences, cat # 00-4506-51) when

775 indicated, for 3 hours. RNA samples were prepared by TRIzol extraction. They were then
776 treated with Turbo DNase (Thermo Fisher, cat # AM2238) for 30 minutes at 37°C and re-
777 purified by phenol:chloroform extraction. 500ng to 1µg RNA was used for reverse
778 transcription using AMV-RT (Promega, cat # M5108) and random 9-mer primer (IDT). cDNA
779 was then quantified by qPCR with iTaq Universal SYBR Mastermix (BioRad, cat # 1725125)
780 and indicated primer pairs. Transcript levels were normalized to 18S.

781 For Figure 2F, equal volume of 4sU RNA eluent were directly reverse transcribed using AMV-
782 RT (Promega) and random 9-mer primer (IDT) and quantified as above with indicated primer
783 pairs. Transcript levels were normalized to spike-in.

784

785 **Western blotting**

786 To prepare whole-cell lysates for evaluating RNase L knock-down murine iBMDMs
787 transfected with RNase L targeting siRNAs (Horizon, cat # L-043480-00-0010), cells were
788 washed with cold DPBS (Gibco) followed by lysis with radioimmunoprecipitation assay (RIPA)
789 lysis buffer (50 mM Tris HCl, 150 mM NaCl, 1.0% [vol/vol] NP-40, 0.5% [wt/vol] sodium
790 deoxycholate, 1.0 mM EDTA, and 0.1% [wt/vol] SDS, Halt™ Protease and Phosphatase
791 Inhibitor Cocktail (Thermo Fisher, cat # PI78440). Cell lysates were vortexed briefly, rotated
792 at 4°C for 15 min, and then clarified by centrifugation at 21,000 × *g* in a tabletop centrifuge at
793 4°C for 10 min to remove debris. 30 µg of whole-cell lysate were resolved on 4% to 15% mini-
794 PROTEAN TGX gels (Bio-Rad). Transfers to polyvinylidene difluoride (PVDF) membranes (Bio-
795 Rad) were done with the Trans-Blot Turbo transfer system (Bio-Rad). Blots were incubated in
796 5% milk in TBS with 0.1% Tween 20 (TBS-T) to block, followed by incubation with primary
797 antibodies against anti-RNase L (Abcam, ab191392, 1:10,000) and anti-GAPDH antibody
798 (abcam ab8245, 1;5,000). Washes were carried out with TBS-T. Blots were then incubated
799 with HRP-conjugated secondary antibodies (Southern Biotechnology, 1:5,000). Washed
800 blots were incubated with Clarity Western ECL substrate (Bio-Rad) for 5 min and visualized
801 with a ChemiDoc imager (Bio-Rad).

802

Statistical analysis

All statistical analyses were performed with GraphPad Prism 10.

Resource Availability

4sU-seq and CUT&RUN-seq datasets were deposited in NCBI Gene Expression Omnibus under the accession numbers GSE298174 and GSE298175, respectively.

Acknowledgements

We thank all members of the Glaunsinger and Coscoy labs for helpful discussions. We thank James Burke and Roy Parker (CU Boulder) for providing the A549 RNaseL KO and complementation cell lines and Susan Carpenter (UC Santa Cruz) for providing the iBMDM cell line. We thank Nharae Eugene Lee for generating the viral stocks used in this study. We thank Alejandro Rivera-Madera for generating the pLJM1-Halo-NLS plasmid used in this study. Imaging was performed at CRL Molecular Imaging Center (RRID:SCR_017852) and the Biological Imaging Facility at UC Berkeley, with special thanks to Holly Aaron and Denise Schichnes for training and technical support. Sequencing of the 4sU-seq samples were performed at Vincent J. Coates Genomics Sequencing Laboratory at UC Berkeley (QB3 Genomics, UC Berkeley, Berkeley, CA, RRID:SCR_022170). Sequencing of the CUT&RUN samples were performed at DNA Technologies and Expression Analysis Core at the UC Davis Genome Center, supported by NIH Shared Instrumentation Grant 1S10OD010786-01. B.G. is an investigator of the Howard Hughes Medical institute and this research was also supported by NIH R01CA136367. Diagrams were created with BioRender.

References

Abernathy, E., Gilbertson, S., Alla, R., Glaunsinger, B., 2015. Viral Nucleases Induce an mRNA Degradation-Transcription Feedback Loop in Mammalian Cells. Cell Host Microbe 18, 243-253.

Andersen, J.B., Mazan-Mamczarz, K., Zhan, M., Gorospe, M., Hassel, B.A., 2009. Ribosomal protein mRNAs are primary targets of regulation in RNase-L-induced senescence. RNA Biol 6, 305-315.

Aprile-Garcia, F., Tomar, P., Hummel, B., Khavaran, A., Sawarkar, R., 2019. Nascent-protein ubiquitination is required for heat shock-induced gene downregulation in human cells. Nat Struct Mol Biol 26, 137-146.

Balsitis, S.J., Coloma, J., Castro, G., Alava, A., Flores, D., McKerrow, J.H., Beatty, P.R., Harris, E., 2009. Tropism of dengue virus in mice and humans defined by viral nonstructural protein 3-specific immunostaining. Am J Trop Med Hyg 80, 416-424.

Banerjee, S., Chakrabarti, A., Jha, B.K., Weiss, S.R., Silverman, R.H., 2014. Cell-type-specific effects of RNase L on viral induction of beta interferon. mBio 5, e00856-00814.

Berry, S., Muller, M., Rai, A., Pelkmans, L., 2022. Feedback from nuclear RNA on transcription promotes robust RNA concentration homeostasis in human cells. Cell Syst 13, 454-470 e415.

Bhat, P., Chow, A., Emert, B., Ettlin, O., Quinodoz, S.A., Strehle, M., Takei, Y., Burr, A., Goronzy, I.N., Chen, A.W., Huang, W., Ferrer, J.L.M., Soehalim, E., Goh, S.T., Chari, T., Sullivan, D.K., Blanco, M.R., Guttman, M., 2024. Genome organization around nuclear speckles drives mRNA splicing efficiency. Nature 629, 1165-1173.

Bolger, A.M., Lohse, M., Usadel, B., 2014. Trimmomatic: a flexible trimmer for Illumina sequence data. Bioinformatics 30, 2114-2120.

Bray, N.L., Pimentel, H., Melsted, P., Pachter, L., 2016. Near-optimal probabilistic RNA-seq quantification. Nat Biotechnol 34, 525-527.

Bregman, D.B., Du, L., van der Zee, S., Warren, S.L., 1995. Transcription-dependent redistribution of the large subunit of RNA polymerase II to discrete nuclear domains. J Cell Biol 129, 287-298.

Bulut-Karslioglu, A., Macrae, T.A., Oses-Prieto, J.A., Covarrubias, S., Percharde, M., Ku, G., Diaz, A., McManus, M.T., Burlingame, A.L., Ramalho-Santos, M., 2018. The Transcriptionally Permissive Chromatin State of Embryonic Stem Cells Is Acutely Tuned to Translational Output. Cell Stem Cell 22, 369-383 e368.

Burke, J.M., Gilchrist, A.R., Sawyer, S.L., Parker, R., 2021. RNase L limits host and viral protein synthesis via inhibition of mRNA export. Sci Adv 7.

Burke, J.M., Moon, S.L., Matheny, T., Parker, R., 2019. RNase L Reprograms Translation by Widespread mRNA Turnover Escaped by Antiviral mRNAs. Mol Cell 75, 1203-1217 e1205.

Burke, J.M., Ripin, N., Ferretti, M.B., St Clair, L.A., Worden-Sapper, E.R., Salgado, F., Sawyer, S.L., Perera, R., Lynch, K.W., Parker, R., 2022. RNase L activation in the cytoplasm induces aberrant processing of mRNAs in the nucleus. PLoS Pathog 18, e1010930.

867 Chapman, R.D., Heidemann, M., Albert, T.K., Mailhammer, R., Flatley, A., Meisterernst, M.,
868 Kremmer, E., Eick, D., 2007. Transcribing RNA polymerase II is phosphorylated at CTD
869 residue serine-7. Science 318, 1780-1782.
870 Chitrakar, A., Rath, S., Donovan, J., Demarest, K., Li, Y., Sridhar, R.R., Weiss, S.R., Kotenko,
871 S.V., Wingreen, N.S., Korennykh, A., 2019. Real-time 2-5A kinetics suggest that interferons
872 beta and lambda evade global arrest of translation by RNase L. Proc Natl Acad Sci U S A
873 116, 2103-2111.
874 Chiu, J., March, P.E., Lee, R., Tillett, D., 2004. Site-directed, Ligase-Independent
875 Mutagenesis (SLIM): a single-tube methodology approaching 100% efficiency in 4 h.
876 Nucleic Acids Res 32, e174.
877 Cusic, R., Burke, J.M., 2024. Condensation of RNase L promotes its rapid activation in
878 response to viral infection in mammalian cells. Sci Signal 17, eadi9844.
879 de Mello, F.N., Tahira, A.C., Berzoti-Coelho, M.G., Verjovski-Almeida, S., 2024. The
880 CUT&RUN greenlist: genomic regions of consistent noise are effective normalizing factors
881 for quantitative epigenome mapping. Brief Bioinform 25.
882 Decker, C.J., Burke, J.M., Mulvaney, P.K., Parker, R., 2022. RNA is required for the integrity of
883 multiple nuclear and cytoplasmic membrane-less RNP granules. EMBO J 41, e110137.
884 Dobin, A., Davis, C.A., Schlesinger, F., Drenkow, J., Zaleski, C., Jha, S., Batut, P., Chaisson,
885 M., Gingeras, T.R., 2013. STAR: ultrafast universal RNA-seq aligner. Bioinformatics 29, 15-
886 21.
887 Donovan, J., Rath, S., Kolet-Mandrikov, D., Korennykh, A., 2017. Rapid RNase L-driven
888 arrest of protein synthesis in the dsRNA response without degradation of translation
889 machinery. RNA 23, 1660-1671.
890 Duncan-Lewis, C., Hartenian, E., King, V., Glaunsinger, B.A., 2021. Cytoplasmic mRNA
891 decay represses RNA polymerase II transcription during early apoptosis. Elife 10.
892 Gaglia, M.M., Covarrubias, S., Wong, W., Glaunsinger, B.A., 2012. A common strategy for
893 host RNA degradation by divergent viruses. J Virol 86, 9527-9530.
894 Gilbertson, S., Federspiel, J.D., Hartenian, E., Cristea, I.M., Glaunsinger, B., 2018. Changes
895 in mRNA abundance drive shuttling of RNA binding proteins, linking cytoplasmic RNA
896 degradation to transcription. Elife 7.
897 Hartenian, E., Gilbertson, S., Federspiel, J.D., Cristea, I.M., Glaunsinger, B.A., 2020. RNA
898 decay during gammaherpesvirus infection reduces RNA polymerase II occupancy of host
899 promoters but spares viral promoters. PLoS Pathog 16, e1008269.
900 Hoboth, P., Sztacho, M., Hozak, P., 2024. Nuclear patterns of phosphatidylinositol 4,5- and
901 3,4-bisphosphate revealed by super-resolution microscopy differ between the consecutive
902 stages of RNA polymerase II transcription. FEBS J 291, 4240-4264.
903 Huai, W., Yang, K., Xing, C., Song, K., Lyu, H., Williams, N.S., Wu, J., Yan, N., 2025. OAS
904 cross-activates RNase L intercellularly through cell-to-cell transfer of 2-5A to spread innate
905 immunity. Immunity 58, 797-810 e796.
906 Iordanov, M.S., Paranjape, J.M., Zhou, A., Wong, J., Williams, B.R., Meurs, E.F., Silverman,
907 R.H., Magun, B.E., 2000. Activation of p38 mitogen-activated protein kinase and c-Jun
908 NH(2)-terminal kinase by double-stranded RNA and encephalomyocarditis virus:
909 involvement of RNase L, protein kinase R, and alternative pathways. Mol Cell Biol 20, 617-
910 627.

Karasik, A., Guydosh, N.R., 2024. The Unusual Role of Ribonuclease L in Innate Immunity. Wiley Interdiscip Rev RNA 15, e1878.
Karasik, A., Lorenzi, H.A., DePass, A.V., Guydosh, N.R., 2024. Endonucleolytic RNA cleavage drives changes in gene expression during the innate immune response. Cell Rep 43, 114287.
Khanna, N., Hu, Y., Belmont, A.S., 2014. HSP70 transgene directed motion to nuclear speckles facilitates heat shock activation. Curr Biol 24, 1138-1144.
Kumar, G.R., Glaunsinger, B.A., 2010. Nuclear import of cytoplasmic poly(A) binding protein restricts gene expression via hyperadenylation and nuclear retention of mRNA. Mol Cell Biol 30, 4996-5008.
Kumar, G.R., Shum, L., Glaunsinger, B.A., 2011. Importin alpha-mediated nuclear import of cytoplasmic poly(A) binding protein occurs as a direct consequence of cytoplasmic mRNA depletion. Mol Cell Biol 31, 3113-3125.
Langmead, B., Salzberg, S.L., 2012. Fast gapped-read alignment with Bowtie 2. Nat Methods 9, 357-359.
Lee, D., Le Pen, J., Yatim, A., Dong, B., Aquino, Y., Ogishi, M., Pescarmona, R., Talouarn, E., Rinchai, D., Zhang, P., Perret, M., Liu, Z., Jordan, I., Elmas Bozdemir, S., Bayhan, G.I., Beaufils, C., Bizien, L., Bisiaux, A., Lei, W., Hasan, M., Chen, J., Gaughan, C., Asthana, A., Libri, V., Luna, J.M., Jaffre, F., Hoffmann, H.H., Michailidis, E., Moreews, M., Seeleuthner, Y., Bilguvar, K., Mane, S., Flores, C., Zhang, Y., Arias, A.A., Bailey, R., Schluter, A., Milisavljevic, B., Bigio, B., Le Voyer, T., Materna, M., Gervais, A., Moncada-Velez, M., Pala, F., Lazarov, T., Levy, R., Neehus, A.L., Rosain, J., Peel, J., Chan, Y.H., Morin, M.P., Pino-Ramirez, R.M., Belkaya, S., Lorenzo, L., Anton, J., Delafontaine, S., Toubiana, J., Bajolle, F., Fumado, V., DeDiego, M.L., Fidouh, N., Rozenberg, F., Perez-Tur, J., Chen, S., Evans, T., Geissmann, F., Lebon, P., Weiss, S.R., Bonnet, D., Duval, X., Co, V.C.C.s.s., sign, C.H.G.E.p., Pan-Hammarstrom, Q., Planas, A.M., Meyts, I., Haerynck, F., Pujol, A., Sancho-Shimizu, V., Dalgard, C.L., Bustamante, J., Puel, A., Boisson-Dupuis, S., Boisson, B., Maniatis, T., Zhang, Q., Bastard, P., Notarangelo, L., Beziat, V., Perez de Diego, R., Rodriguez-Gallego, C., Su, H.C., Lifton, R.P., Jouanguy, E., Cobat, A., Alsina, L., Keles, S., Haddad, E., Abel, L., Belot, A., Quintana-Murci, L., Rice, C.M., Silverman, R.H., Zhang, S.Y., Casanova, J.L., 2023. Inborn errors of OAS-RNase L in SARS-CoV-2-related multisystem inflammatory syndrome in children. Science 379, eabo3627.
Lee, Y.J., Glaunsinger, B.A., 2009. Aberrant herpesvirus-induced polyadenylation correlates with cellular messenger RNA destruction. PLoS Biol 7, e1000107.
Li, H.B., Tong, J., Zhu, S., Batista, P.J., Duffy, E.E., Zhao, J., Bailis, W., Cao, G., Kroehling, L., Chen, Y., Wang, G., Broughton, J.P., Chen, Y.G., Kluger, Y., Simon, M.D., Chang, H.Y., Yin, Z., Flavell, R.A., 2017. m(6)A mRNA methylation controls T cell homeostasis by targeting the IL-7/STAT5/SOCS pathways. Nature 548, 338-342.
Liao, Y., Smyth, G.K., Shi, W., 2014. featureCounts: an efficient general purpose program for assigning sequence reads to genomic features. Bioinformatics 30, 923-930.
Liu, N., Hargreaves, V.V., Zhu, Q., Kurland, J.V., Hong, J., Kim, W., Sher, F., Macias-Trevino, C., Rogers, J.M., Kurita, R., Nakamura, Y., Yuan, G.C., Bauer, D.E., Xu, J., Bulyk, M.L., Orkin, S.H., 2018a. Direct Promoter Repression by BCL11A Controls the Fetal to Adult Hemoglobin Switch. Cell 173, 430-442 e417.

Liu, X., Fu, R., Pan, Y., Meza-Sosa, K.F., Zhang, Z., Lieberman, J., 2018b. PNPT1 Release from Mitochondria during Apoptosis Triggers Decay of Poly(A) RNAs. Cell 174, 187-201 e112.

Malathi, K., Dong, B., Gale, M., Jr., Silverman, R.H., 2007. Small self-RNA generated by RNase L amplifies antiviral innate immunity. Nature 448, 816-819.

Miura, M., Chen, H., 2020. CUT&RUN detects distinct DNA footprints of RNA polymerase II near the transcription start sites. Chromosome Res 28, 381-393.

Morgens, D.W., Gulyas, L., Mao, X., Rivera-Madera, A., Souza, A.S., Glaunsinger, B.A., 2025. Enhancers and genome conformation provide complex transcriptional control of a herpesviral gene. Mol Syst Biol 21, 30-58.

Niu, T.K., Pfeifer, A.C., Lippincott-Schwartz, J., Jackson, C.L., 2005. Dynamics of GBF1, a Brefeldin A-sensitive Arf1 exchange factor at the Golgi. Mol Biol Cell 16, 1213-1222.

Radle, B., Rutkowski, A.J., Ruzsics, Z., Friedel, C.C., Koszinowski, U.H., Dolken, L., 2013. Metabolic labeling of newly transcribed RNA for high resolution gene expression profiling of RNA synthesis, processing and decay in cell culture. J Vis Exp.

Ramirez, F., Ryan, D.P., Gruning, B., Bhardwaj, V., Kilpert, F., Richter, A.S., Heyne, S., Dundar, F., Manke, T., 2016. deepTools2: a next generation web server for deep-sequencing data analysis. Nucleic Acids Res 44, W160-165.

Rath, S., Prangley, E., Donovan, J., Demarest, K., Wingreen, N.S., Meir, Y., Korennykh, A., 2019. Concerted 2-5A-Mediated mRNA Decay and Transcription Reprogram Protein Synthesis in the dsRNA Response. Mol Cell 75, 1218-1228 e1216.

Ritchie, M.E., Phipson, B., Wu, D., Hu, Y., Law, C.W., Shi, W., Smyth, G.K., 2015. limma powers differential expression analyses for RNA-sequencing and microarray studies. Nucleic Acids Res 43, e47.

Ross-Innes, C.S., Stark, R., Teschendorff, A.E., Holmes, K.A., Ali, H.R., Dunning, M.J., Brown, G.D., Gojis, O., Ellis, I.O., Green, A.R., Ali, S., Chin, S.F., Palmieri, C., Caldas, C., Carroll, J.S., 2012. Differential oestrogen receptor binding is associated with clinical outcome in breast cancer. Nature 481, 389-393.

Sancak, Y., Peterson, T.R., Shaul, Y.D., Lindquist, R.A., Thoreen, C.C., Bar-Peled, L., Sabatini, D.M., 2008. The Rag GTPases bind raptor and mediate amino acid signaling to mTORC1. Science 320, 1496-1501.

Shore, D., Albert, B., 2022. Ribosome biogenesis and the cellular energy economy. Curr Biol 32, R611-R617.

Siddiqui, M.A., Malathi, K., 2012. RNase L induces autophagy via c-Jun N-terminal kinase and double-stranded RNA-dependent protein kinase signaling pathways. J Biol Chem 287, 43651-43664.

Slomnicki, L.P., Chung, D.H., Parker, A., Hermann, T., Boyd, N.L., Hetman, M., 2017. Ribosomal stress and Tp53-mediated neuronal apoptosis in response to capsid protein of the Zika virus. Sci Rep 7, 16652.

Smith, T., Heger, A., Sudbery, I., 2017. UMI-tools: modeling sequencing errors in Unique Molecular Identifiers to improve quantification accuracy. Genome Res 27, 491-499.

Takenaka, Y., Yamada, A., Tomioka, Y., Akiyama, Y., Ivanov, P., 2025. RNase L Produces tRNA-derived RNAs that Contribute to Translation Inhibition. RNA.

Thomas, M.P., Liu, X., Whangbo, J., McCrossan, G., Sanborn, K.B., Basar, E., Walch, M., Lieberman, J., 2015. Apoptosis Triggers Specific, Rapid, and Global mRNA Decay with 3' Uridylated Intermediates Degraded by DIS3L2. Cell Rep 11, 1079-1089.

Watkins, J.M., Burke, J.M., 2024. RNase L-induced bodies sequester subgenomic flavivirus RNAs to promote viral RNA decay. Cell Rep 43, 114694.

Whelan, J.N., Li, Y., Silverman, R.H., Weiss, S.R., 2019. Zika Virus Production Is Resistant to RNase L Antiviral Activity. J Virol 93.

Whelan, J.N., Parenti, N.A., Hatterschide, J., Renner, D.M., Li, Y., Reyes, H.M., Dong, B., Perez, E.R., Silverman, R.H., Weiss, S.R., 2021. Zika virus employs the host antiviral RNase L protein to support replication factory assembly. Proc Natl Acad Sci U S A 118.

Wu, J., Xiao, Y., Liu, Y., Wen, L., Jin, C., Liu, S., Paul, S., He, C., Regev, O., Fei, J., 2024. Dynamics of RNA localization to nuclear speckles are connected to splicing efficiency. Sci Adv 10, eadp7727.

Xi, J., Snieckute, G., Martinez, J.F., Arendrup, F.S.W., Asthana, A., Gaughan, C., Lund, A.H., Bekker-Jensen, S., Silverman, R.H., 2024. Initiation of a ZAKalpha-dependent ribotoxic stress response by the innate immunity endoribonuclease RNase L. Cell Rep 43, 113998.

Xie, S.Q., Martin, S., Guillot, P.V., Bentley, D.L., Pombo, A., 2006. Splicing speckles are not reservoirs of RNA polymerase II, but contain an inactive form, phosphorylated on serine2 residues of the C-terminal domain. Mol Biol Cell 17, 1723-1733.

Yang, K., Dong, B., Asthana, A., Silverman, R.H., Yan, N., 2024. RNA helicase SKIV2L limits antiviral defense and autoinflammation elicited by the OAS-RNase L pathway. EMBO J 43, 3876-3894.

Zhu, Z., Liu, J., Feng, H., Zhang, Y., Huang, R., Pan, Q., Nan, J., Miao, R., Cheng, B., 2022. Overcoming the cytoplasmic retention of GDOWN1 modulates global transcription and facilitates stress adaptation. Elife 11.

Figure 1

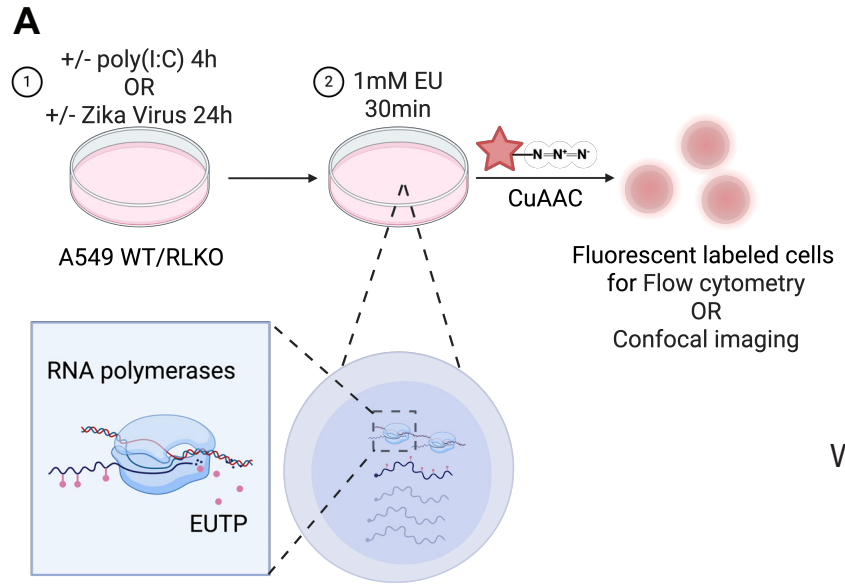
A
① +/- poly(I:C) 4h
OR
+/- Zika Virus 24h
② 1mM EU
30min
CuAAC
A549 WT/RLKO
Fluorescent labeled cells
for Flow cytometry
OR
Confocal imaging
RNA polymerases
EUTP

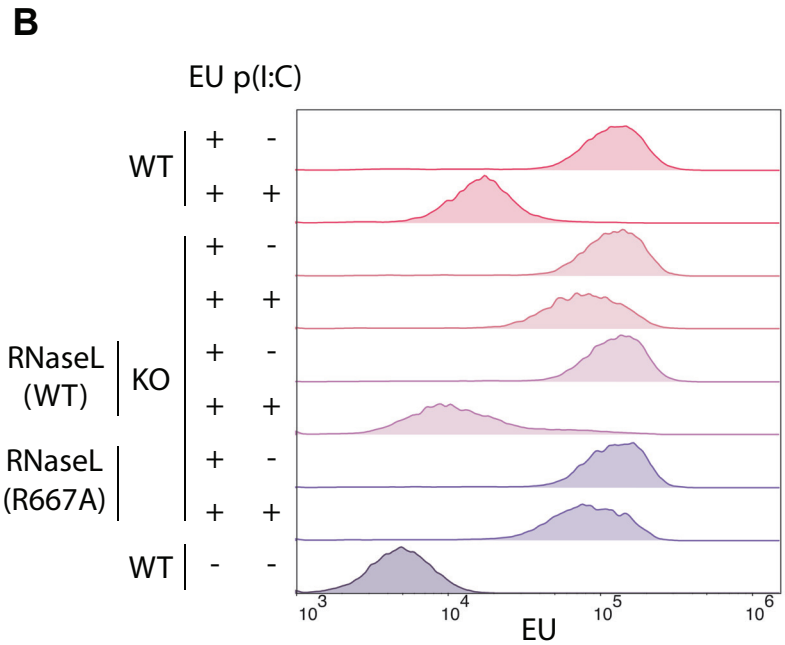
B
EU p(I:C)
WT
RNaseL (WT)
KO
RNaseL (R667A)
WT
EU

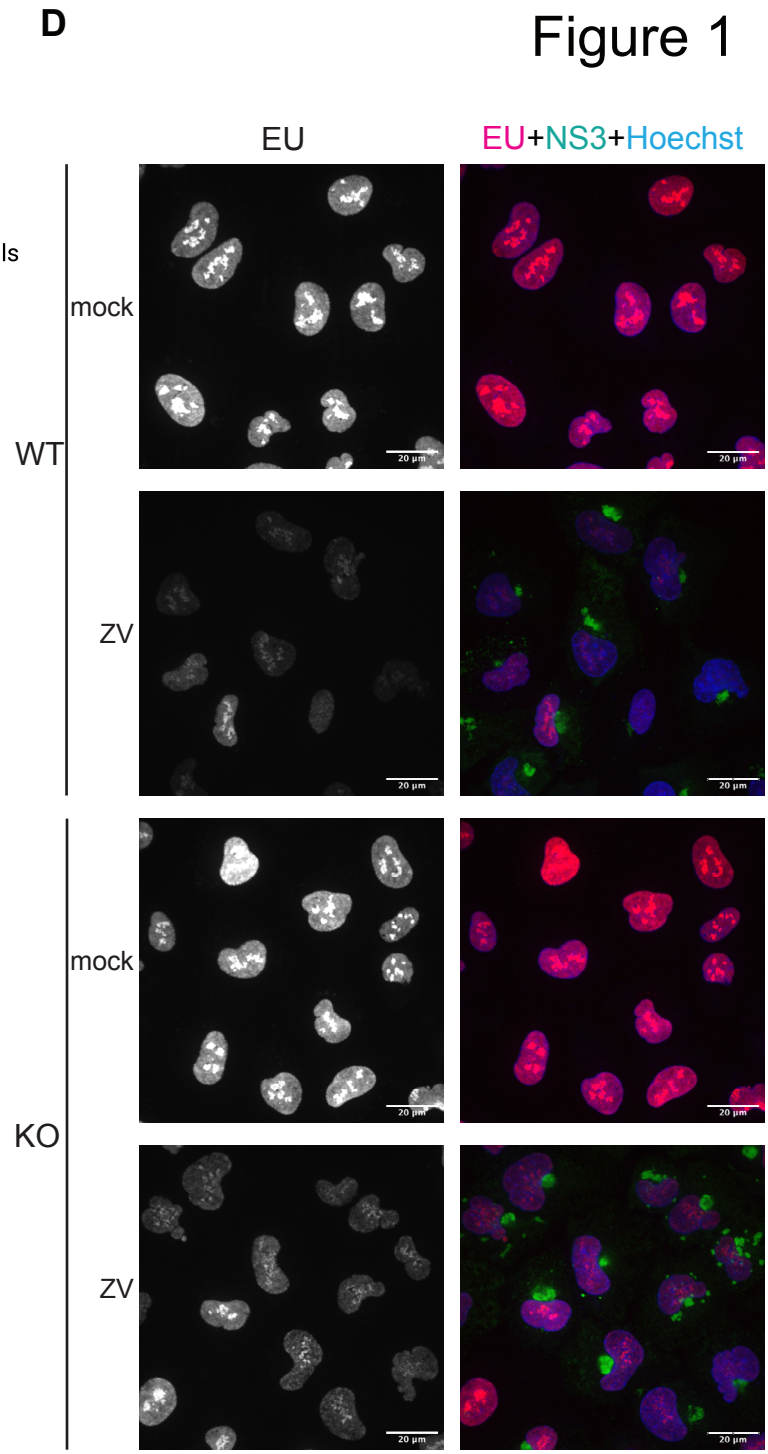
D
EU
EU+NS3+Hoechst
mock
ZV
WT
mock
ZV
KO

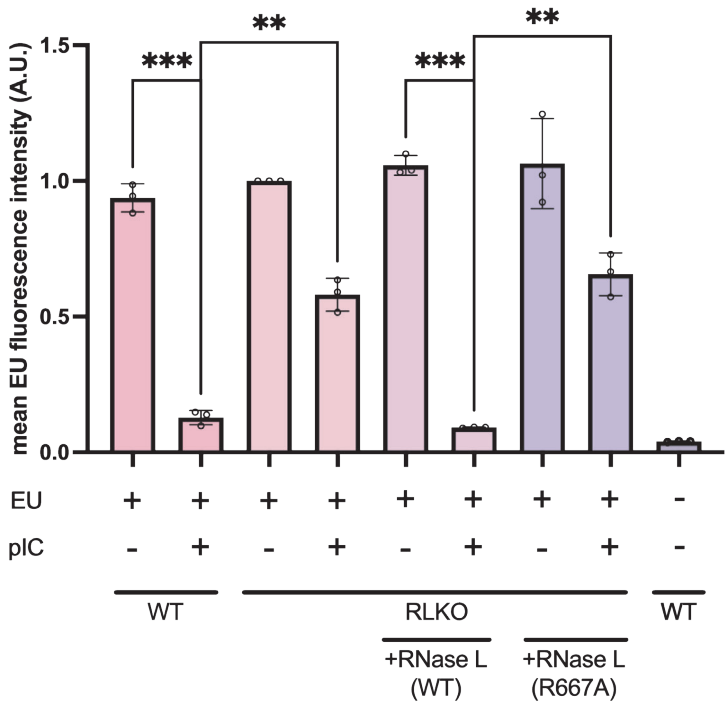
C
mean EU fluorescence intensity (A.U.)
EU
pIC
WT
RLKO
+RNase L (WT)
+RNase L (R667A)
WT

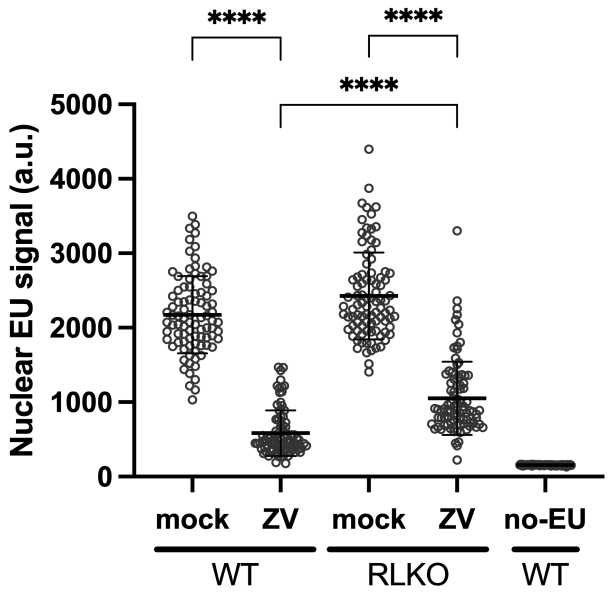
E
Nuclear EU signal (a.u.)
mock
ZV
mock
ZV
no-EU
WT
RLKO
WT

Figure 2

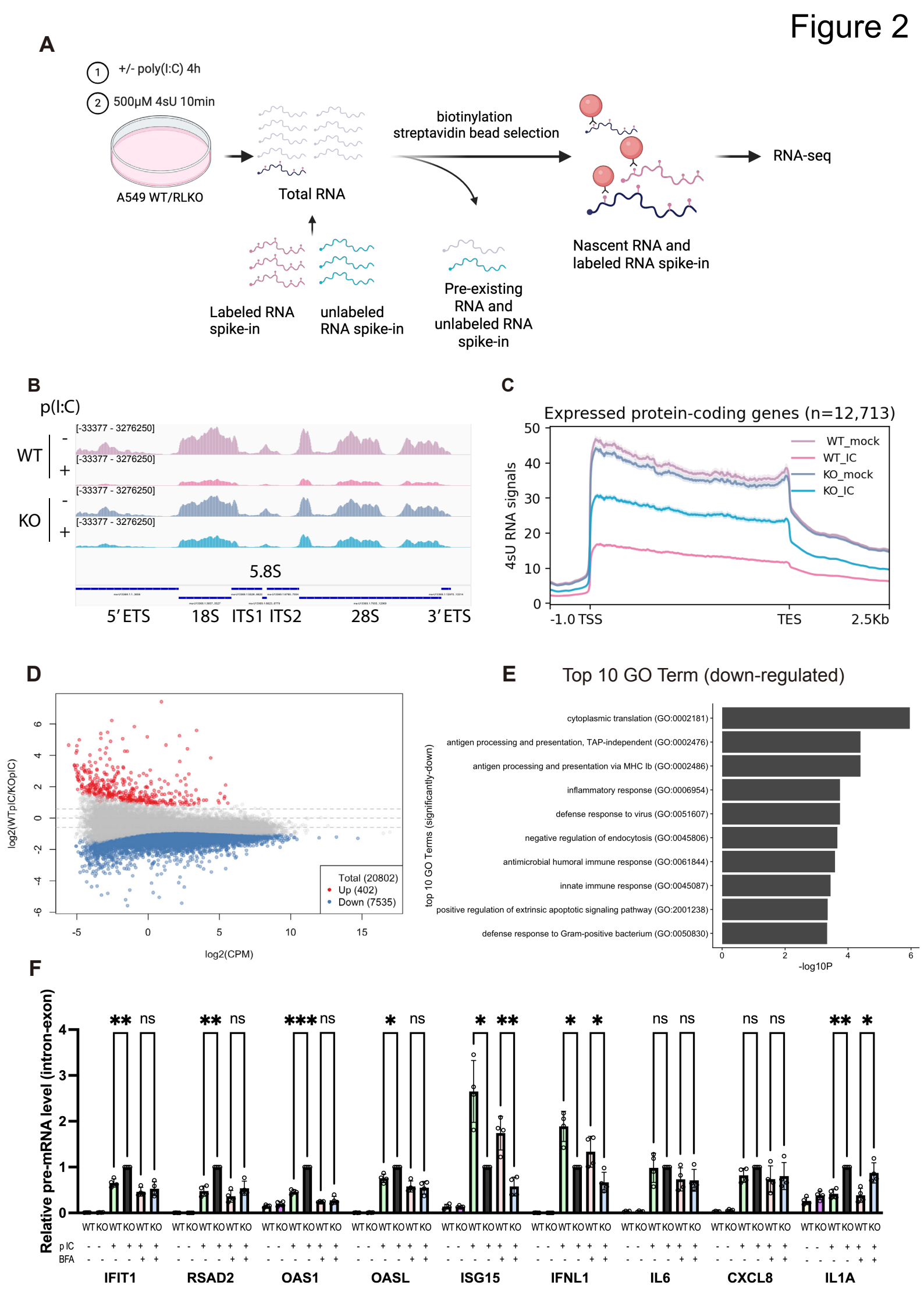
A
1 +/- poly(I:C) 4h
2 500μM 4sU 10min
A549 WT/RLKO
Total RNA
biotinylation
streptavidin bead selection
RNA-seq
Nascent RNA and
labeled RNA spike-in
Labeled RNA
spike-in
unlabeled
RNA spike-in
Pre-existing
RNA and
unlabeled RNA
spike-in
B
p(I:C)
WT
KO
[-33377 - 3276250]
5.8S
5′ETS
18S
ITS1
ITS2
28S
3′ETS
C
Expressed protein-coding genes (n=12,713)
4sU RNA signals
WT_mock
WT_IC
KO_mock
KO_IC
-1.0 TSS
TES
2.5Kb
D
log2(WTpIC/KOpIC)
log2(CPM)
Total (20802)
Up (402)
Down (7535)
E
Top 10 GO Term (down-regulated)
top 10 GO Terms (significantly-down)
cytoplasmic translation (GO:0002181)
antigen processing and presentation, TAP-independent (GO:0002476)
antigen processing and presentation via MHC Ib (GO:0002486)
inflammatory response (GO:0006954)
defense response to virus (GO:0051607)
negative regulation of endocytosis (GO:0045806)
antimicrobial humoral immune response (GO:0061844)
innate immune response (GO:0045087)
positive regulation of extrinsic apoptotic signaling pathway (GO:2001238)
defense response to Gram-positive bacterium (GO:0050830)
-log10P
F
Relative pre-mRNA level (intron-exon)
WT KO WT KO WT KO
pIC
BFA
IFIT1
RSAD2
OAS1
OASL
ISG15
IFNL1
IL6
CXCL8
IL1A

Figure 3

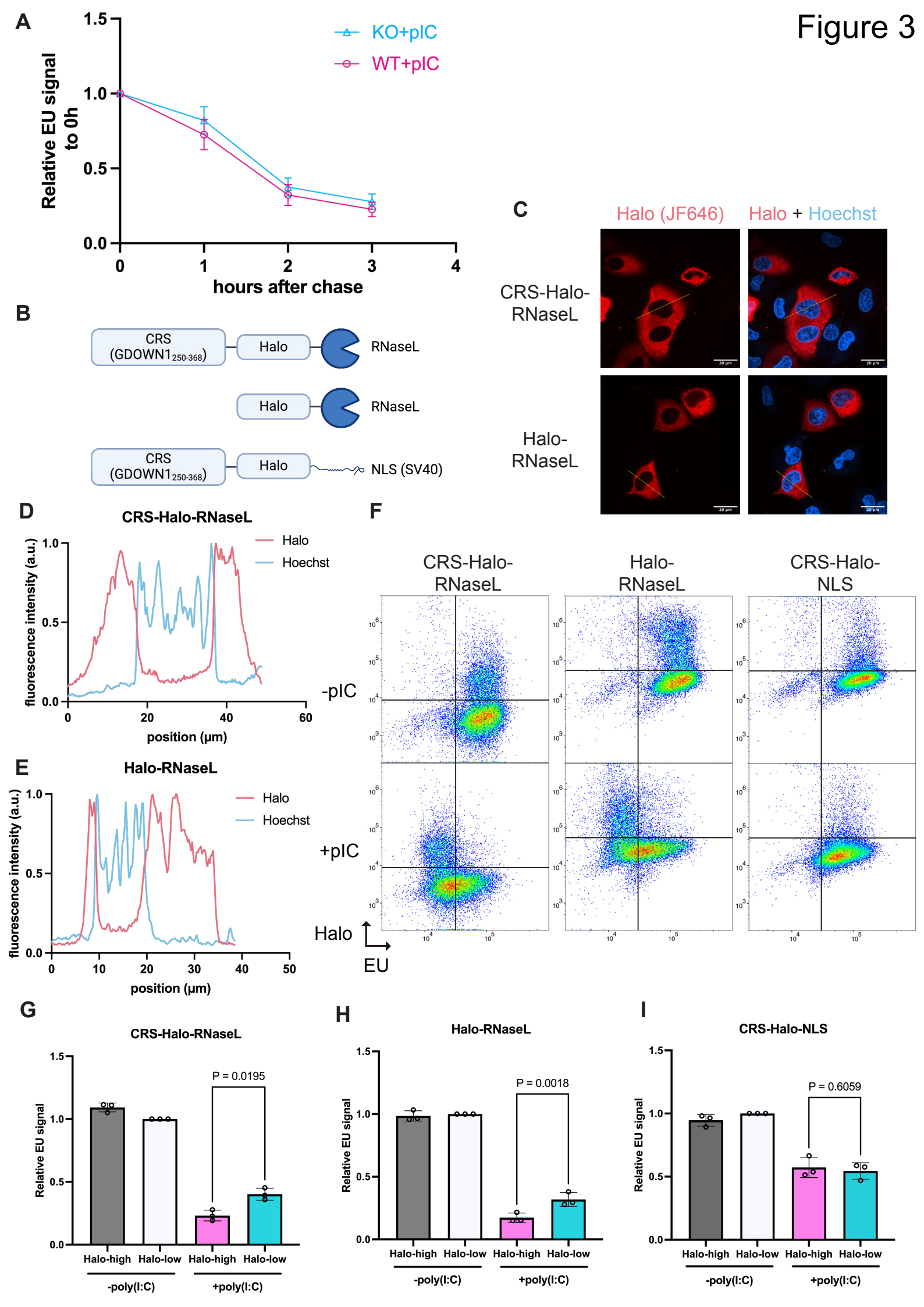
A
KO+pIC
WT+pIC
Relative EU signal to 0h
hours after chase
B
CRS (GDOWN1250-368)
Halo
RNaseL
NLS (SV40)
C
Halo (JF646)
Halo + Hoechst
CRS-Halo-RNaseL
Halo-RNaseL
D
CRS-Halo-RNaseL
Halo
Hoechst
fluorescence intensity (a.u.)
position (µm)
E
Halo-RNaseL
F
CRS-Halo-RNaseL
Halo-RNaseL
CRS-Halo-NLS
-pIC
+pIC
Halo
EU
G
CRS-Halo-RNaseL
P = 0.0195
Relative EU signal
Halo-high
Halo-low
-poly(I:C)
+poly(I:C)
H
Halo-RNaseL
P = 0.0018
I
CRS-Halo-NLS
P = 0.6059

Figure 4

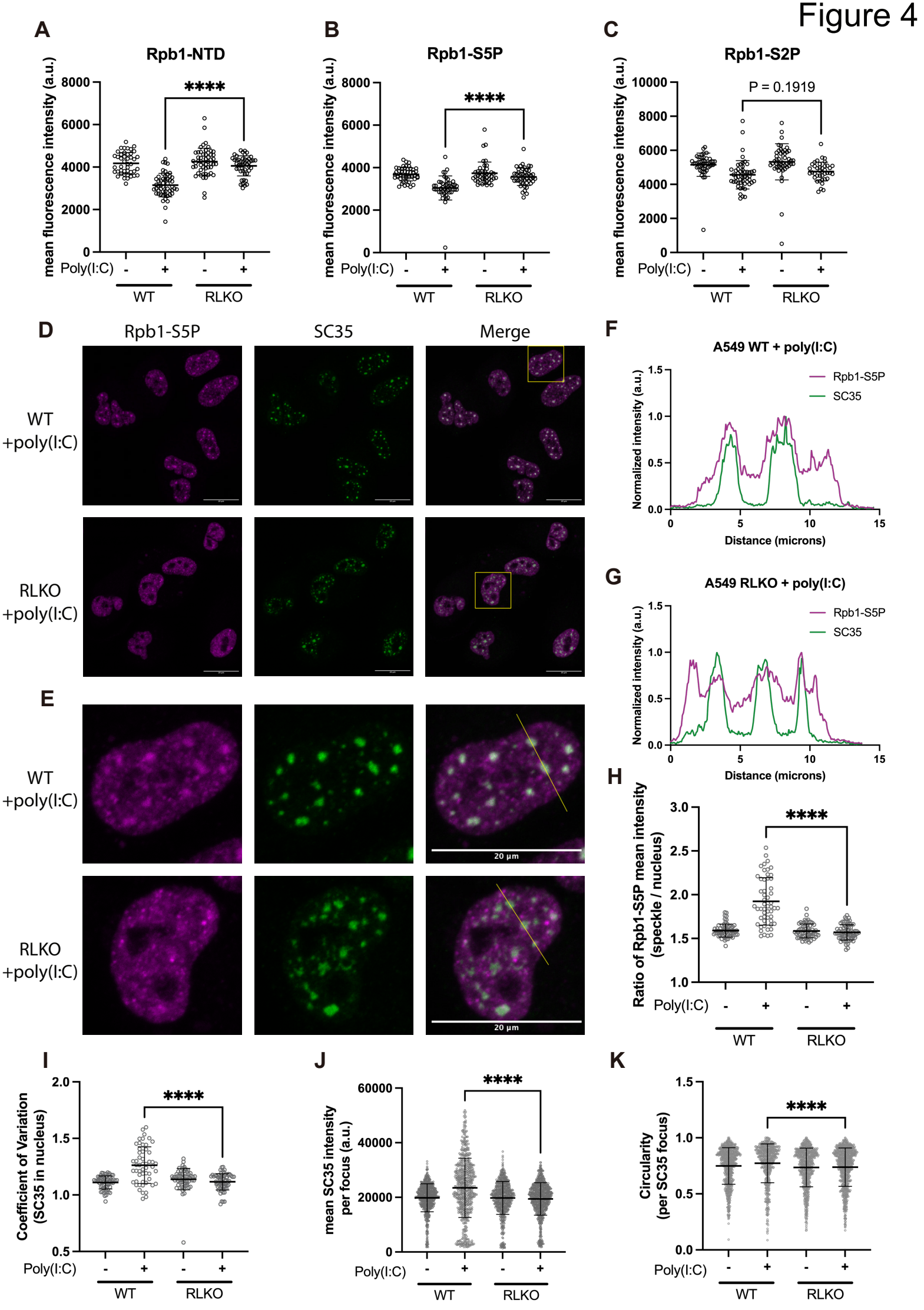
A
Rpb1-NTD
mean fluorescence intensity (a.u.)
8000
6000
4000
2000
0
****
Poly(I:C) - + - +
WT
RLKO
B
Rpb1-S5P
mean fluorescence intensity (a.u.)
8000
6000
4000
2000
0
****
Poly(I:C) - + - +
WT
RLKO
C
Rpb1-S2P
mean fluorescence intensity (a.u.)
10000
8000
6000
4000
2000
0
P = 0.1919
Poly(I:C) - + - +
WT
RLKO
D
Rpb1-S5P
SC35
Merge
WT
+poly(I:C)
RLKO
+poly(I:C)
E
WT
+poly(I:C)
RLKO
+poly(I:C)
20 µm
20 µm
F
A549 WT + poly(I:C)
Rpb1-S5P
SC35
Normalized intensity (a.u.)
1.5
1.0
0.5
0.0
0
5
10
15
Distance (microns)
G
A549 RLKO + poly(I:C)
Rpb1-S5P
SC35
Normalized intensity (a.u.)
1.5
1.0
0.5
0.0
0
5
10
15
Distance (microns)
H
Ratio of Rpb1-S5P mean intensity
(speckle / nucleus)
3.0
2.5
2.0
1.5
1.0
****
Poly(I:C) - + - +
WT
RLKO
I
Coefficient of Variation
(SC35 in nucleus)
2.0
1.5
1.0
0.5
****
Poly(I:C) - + - +
WT
RLKO
J
mean SC35 intensity
per focus (a.u.)
60000
40000
20000
0
****
Poly(I:C) - + - +
WT
RLKO
K
Circularity
(per SC35 focus)
1.5
1.0
0.5
0.0
****
Poly(I:C) - + - +
WT
RLKO

Figure 5

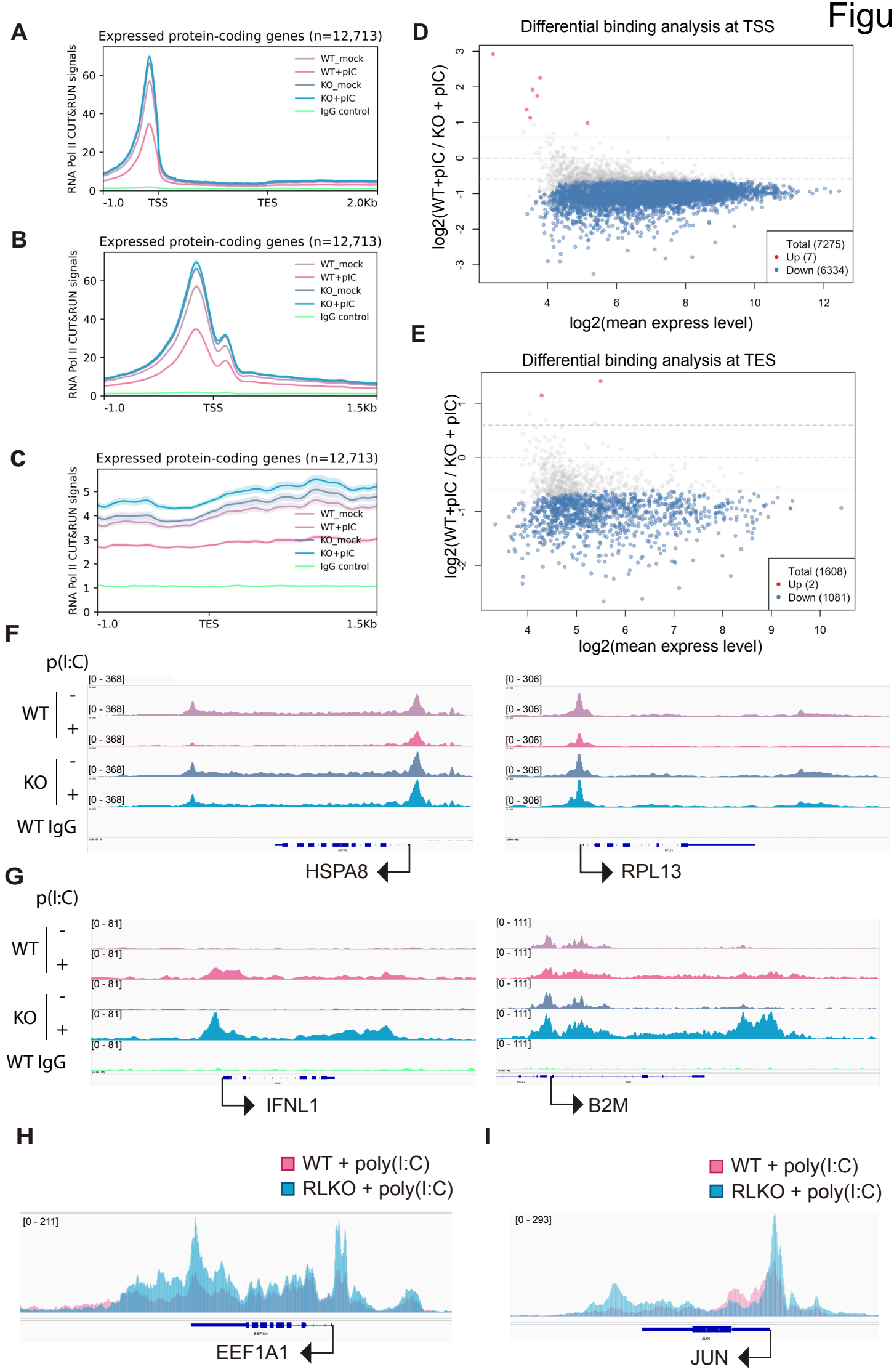
A
Expressed protein-coding genes (n=12,713)
RNA Pol II CUT&RUN signals
WT_mock
WT+pIC
KO_mock
KO+pIC
IgG control
-1.0
TSS
TES
2.0Kb
B
Expressed protein-coding genes (n=12,713)
RNA Pol II CUT&RUN signals
-1.0
TSS
1.5Kb
C
Expressed protein-coding genes (n=12,713)
RNA Pol II CUT&RUN signals
-1.0
TES
1.5Kb
D
Differential binding analysis at TSS
log2(WT+pIC / KO + pIC)
log2(mean express level)
Total (7275)
Up (7)
Down (6334)
E
Differential binding analysis at TES
log2(WT+pIC / KO + pIC)
log2(mean express level)
Total (1608)
Up (2)
Down (1081)
F
p(I:C)
WT
KO
WT IgG
HSPA8
RPL13
G
p(I:C)
WT
KO
WT IgG
IFNL1
B2M
H
WT + poly(I:C)
RLKO + poly(I:C)
EEF1A1
I
WT + poly(I:C)
RLKO + poly(I:C)
JUN

Figure S1

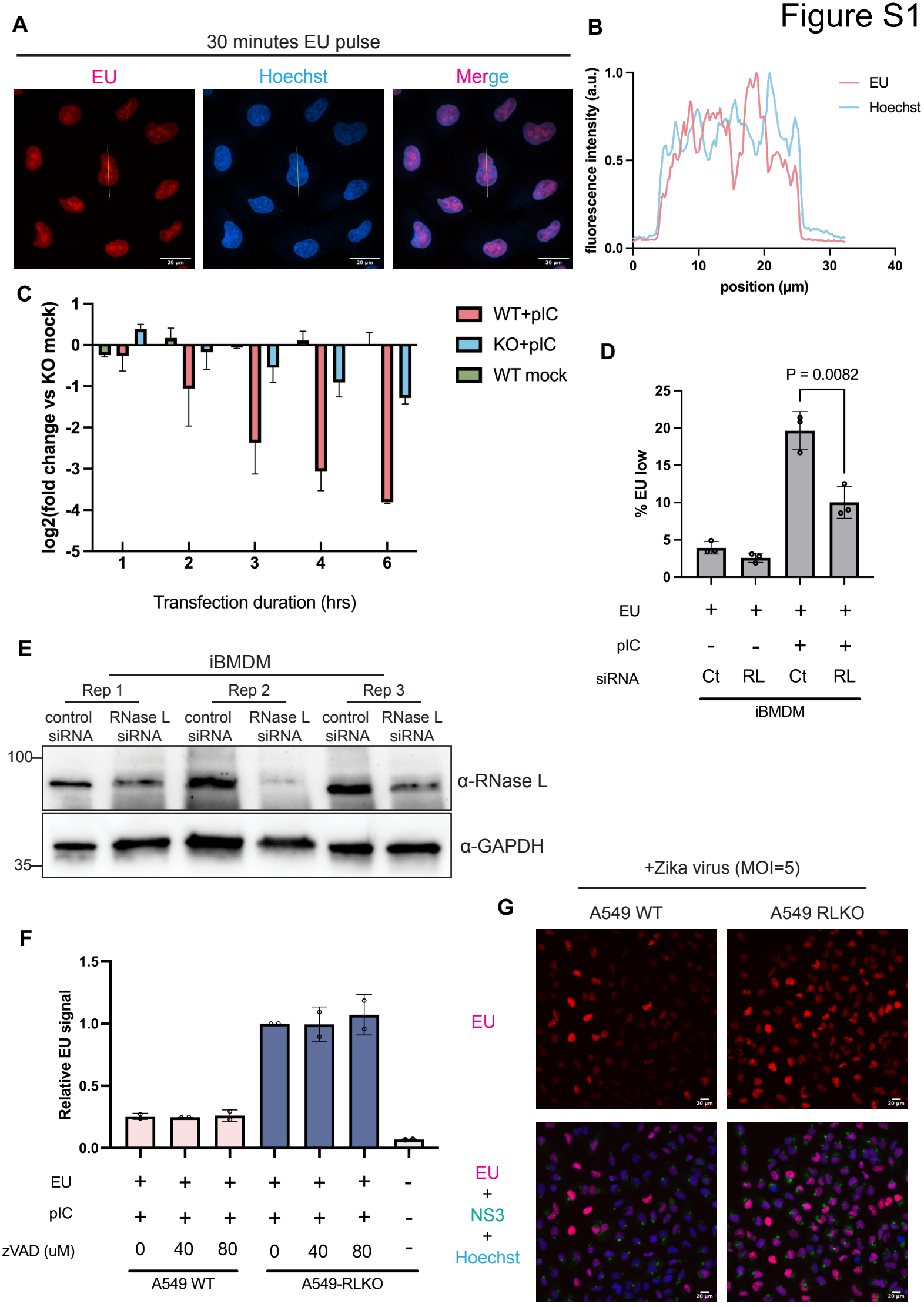
A
30 minutes EU pulse
EU
Hoechst
Merge
B
fluorescence intensity (a.u.)
position (μm)
EU
Hoechst
C
log2(fold change vs KO mock)
Transfection duration (hrs)
WT+pIC
KO+pIC
WT mock
D
P = 0.0082
% EU low
EU
pIC
siRNA
Ct
RL
iBMDM
E
iBMDM
Rep 1
Rep 2
Rep 3
control siRNA
RNase L siRNA
α-RNase L
α-GAPDH
F
Relative EU signal
EU
pIC
zVAD (uM)
A549 WT
A549-RLKO
G
+Zika virus (MOI=5)
A549 WT
A549 RLKO
EU
EU + NS3 + Hoechst

Figure S2

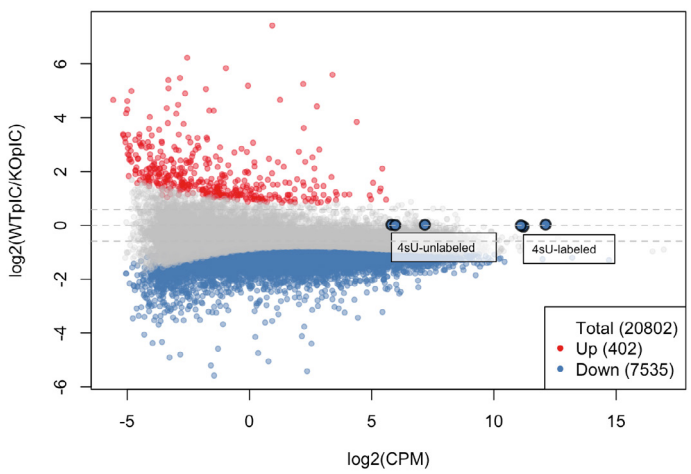
A
log2(WTpIC/KOpIC)
log2(CPM)
4sU-unlabeled
4sU-labeled
Total (20802)
Up (402)
Down (7535)

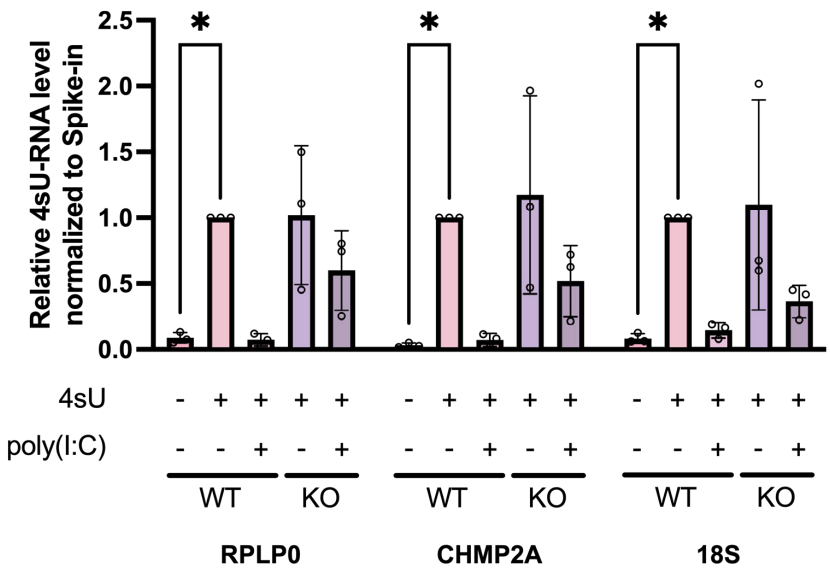
B
Relative 4sU-RNA level normalized to Spike-in
4sU
poly(I:C)
WT
KO
RPLP0
CHMP2A
18S

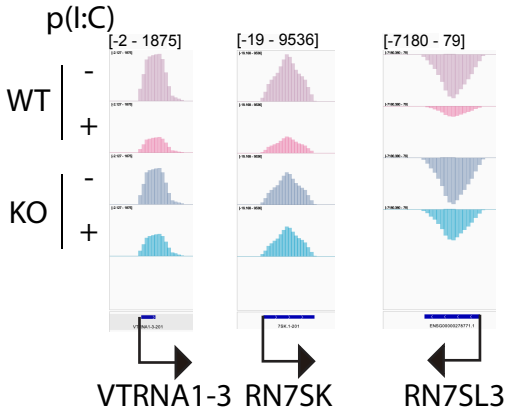
C
p(I:C)
WT
KO
[-2 - 1875]
[-19 - 9536]
[-7180 - 79]
VTRNA1-3
RN7SK
RN7SL3

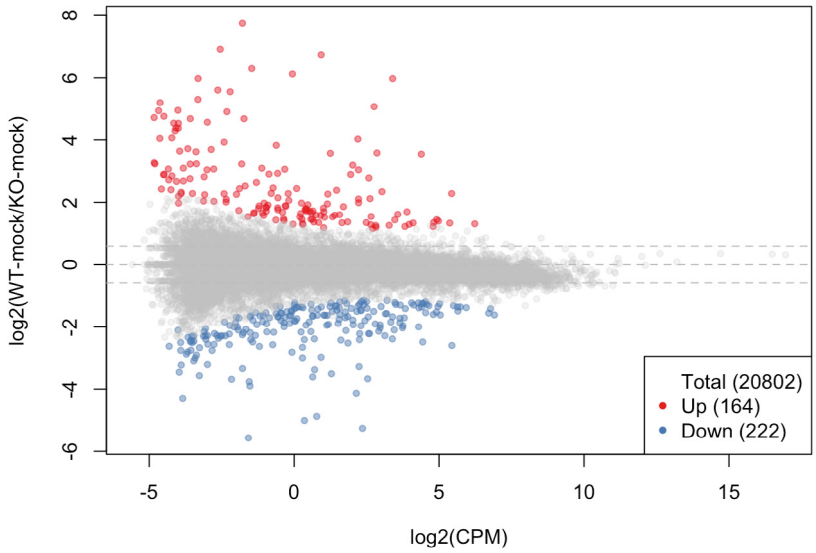
D
log2(WT-mock/KO-mock)
log2(CPM)
Total (20802)
Up (164)
Down (222)

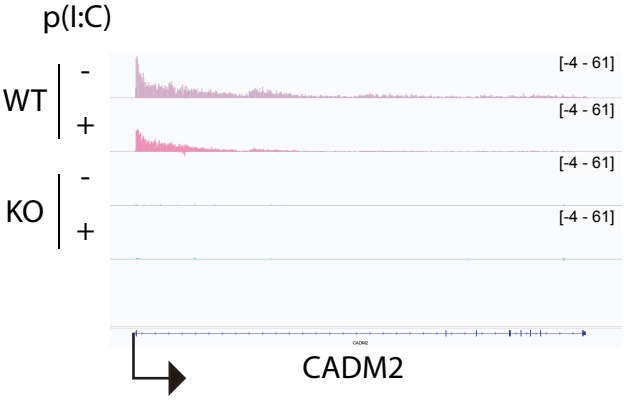
E
p(I:C)
WT
KO
[-4 - 61]
CADM2

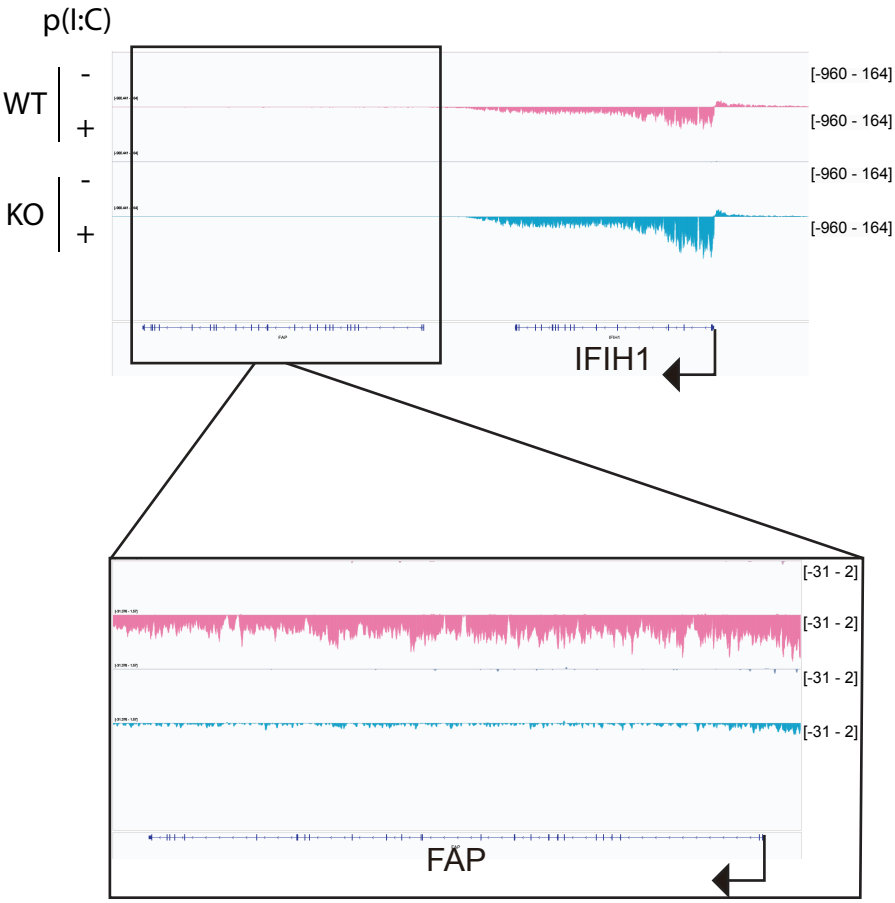
F
p(I:C)
WT
KO
[-960 - 164]
IFIH1
[-31 - 2]
FAP

Figure S3

A

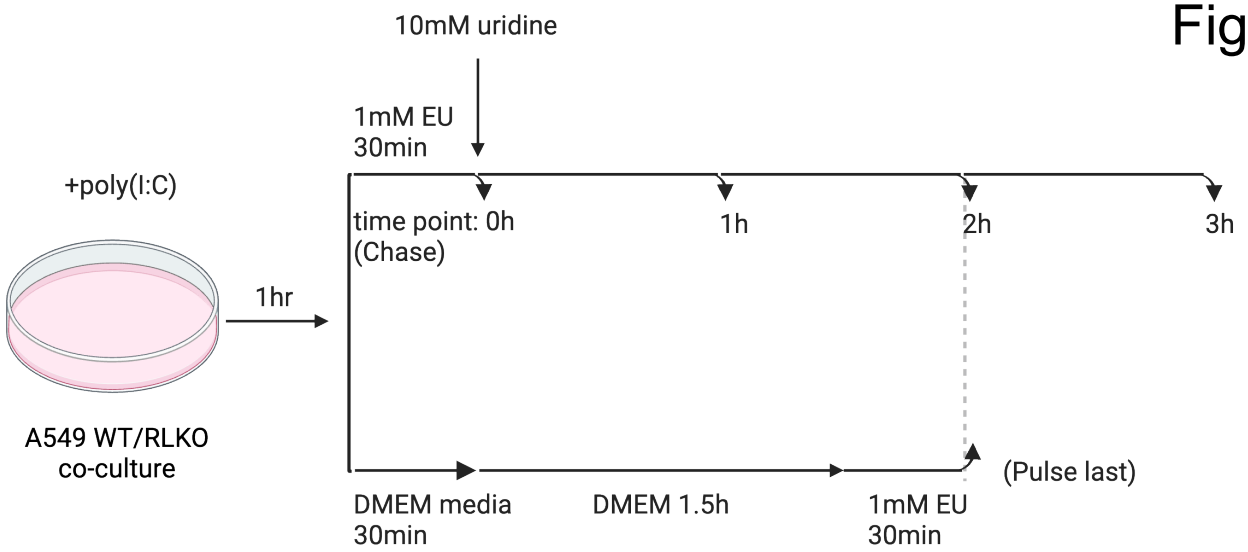

B

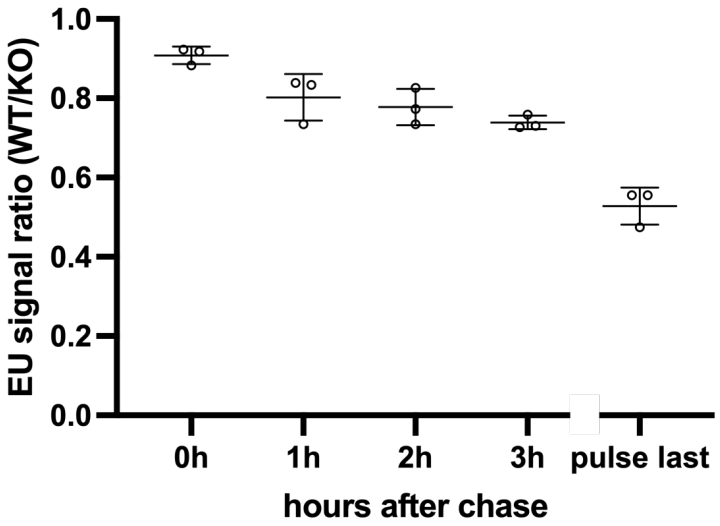

C

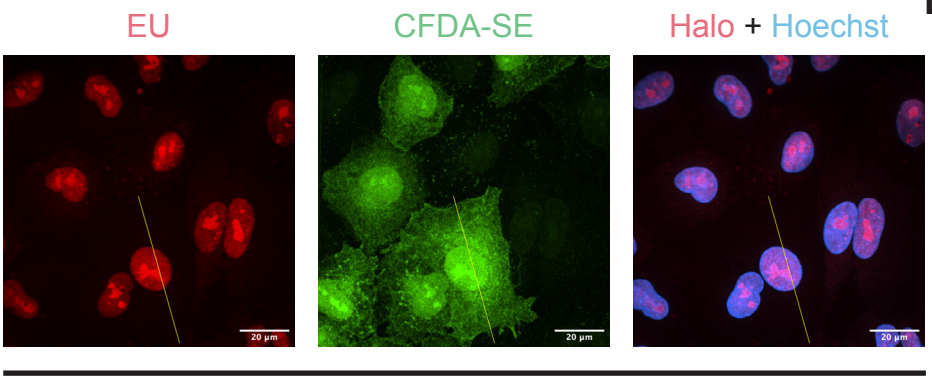

+poly (I:C)
2h chase

D

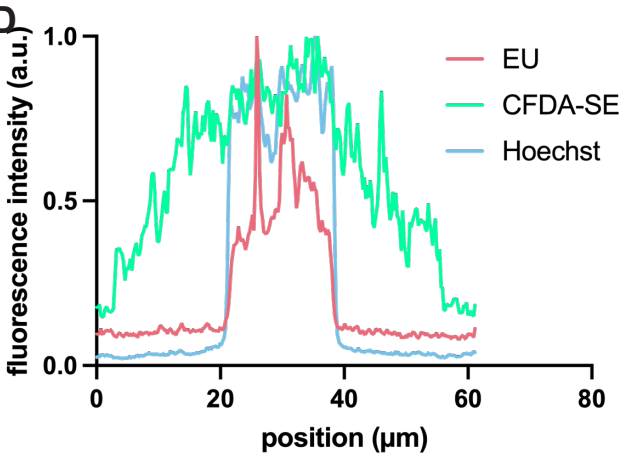

E

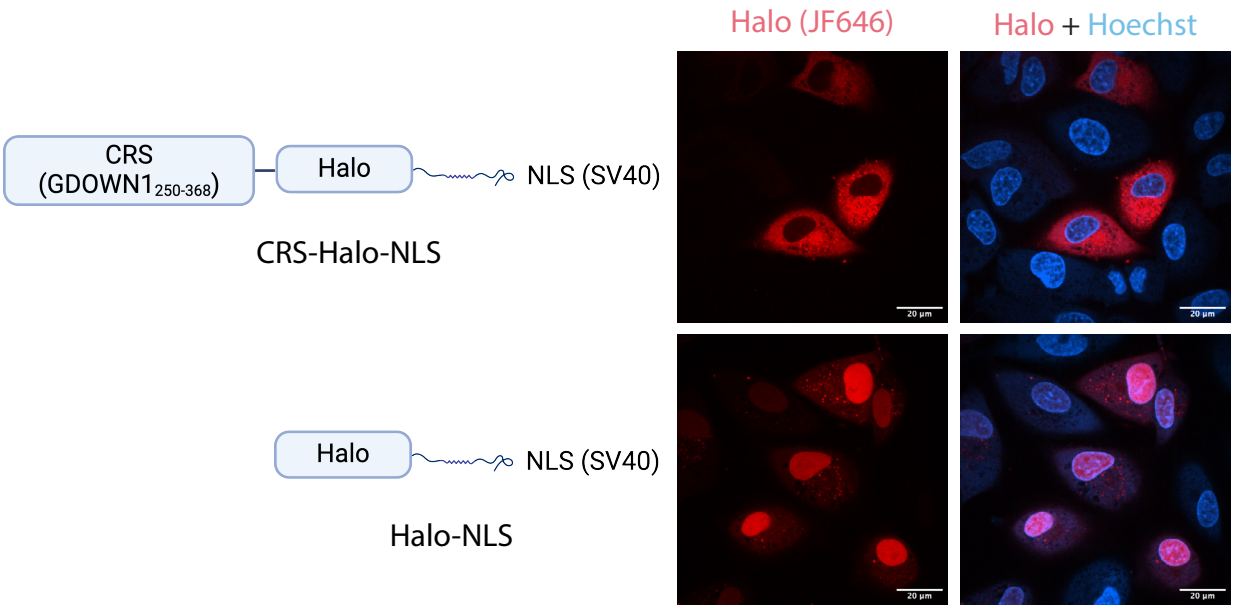

Figure S4

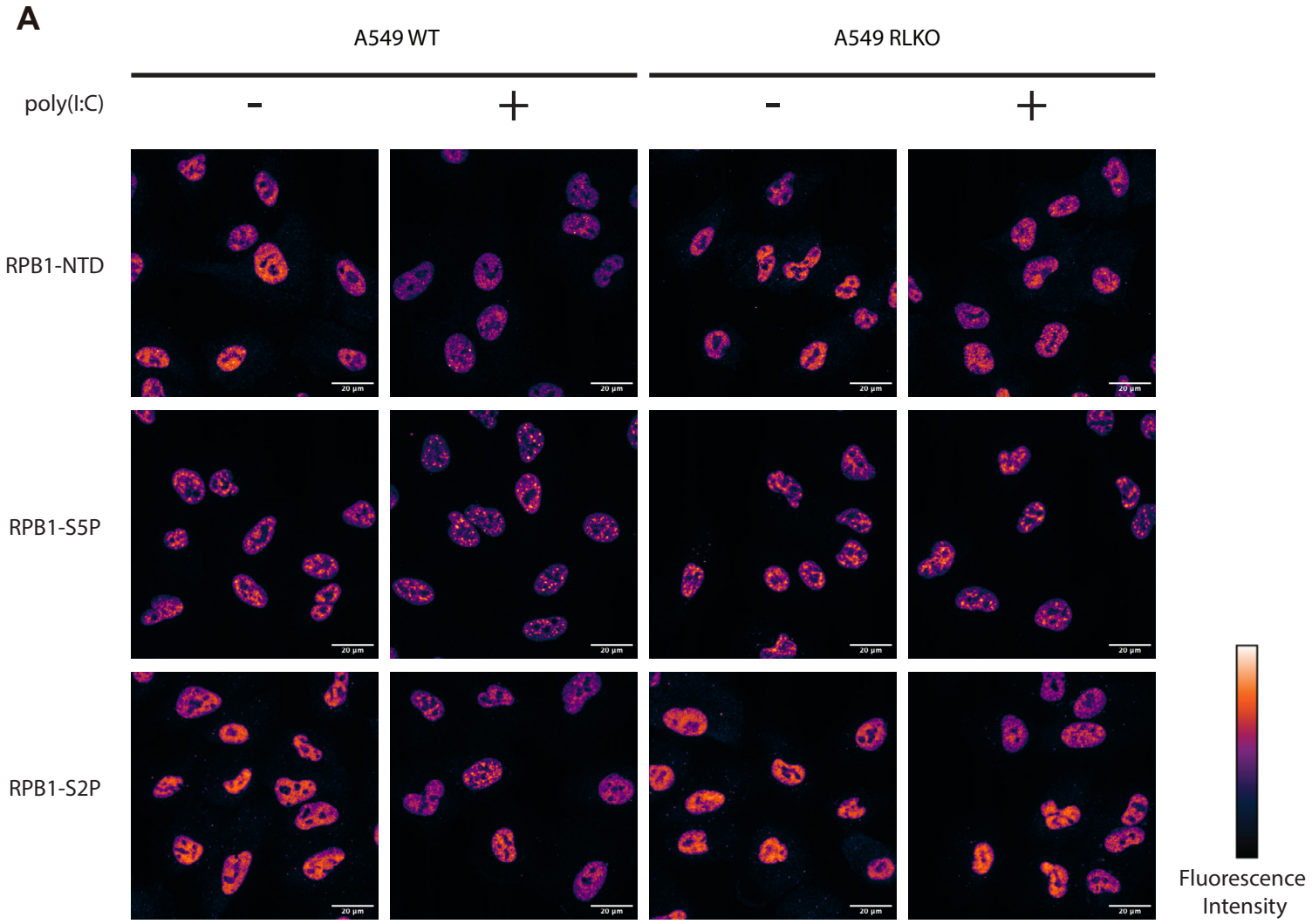
A
A549 WT
A549 RLKO
poly(I:C)
-
+
-
+
RPB1-NTD
RPB1-S5P
RPB1-S2P
Fluorescence Intensity

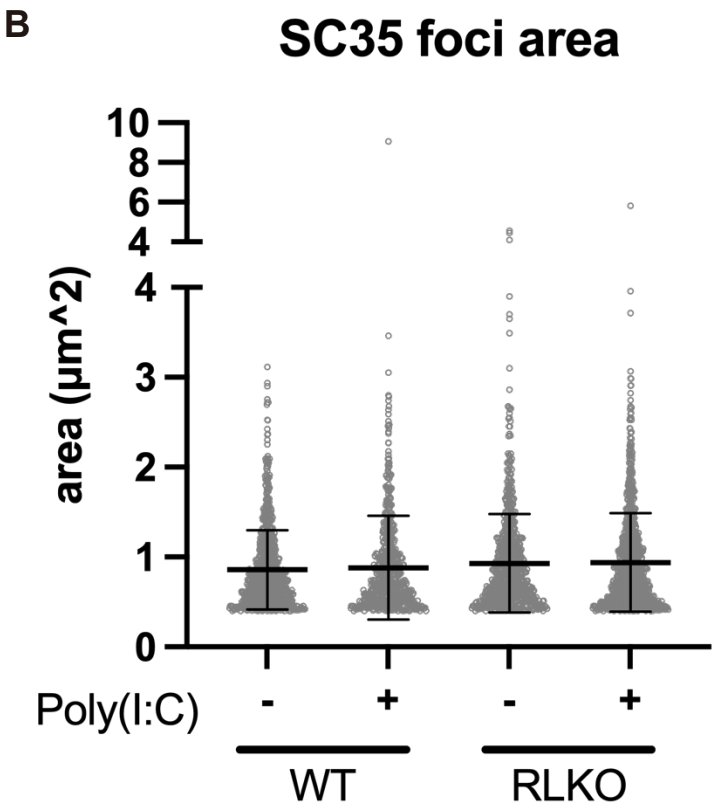
B
SC35 foci area
area (µm^2)
10
8
6
4
4
3
2
1
0
Poly(I:C)
-
+
-
+
WT
RLKO

Figure S5

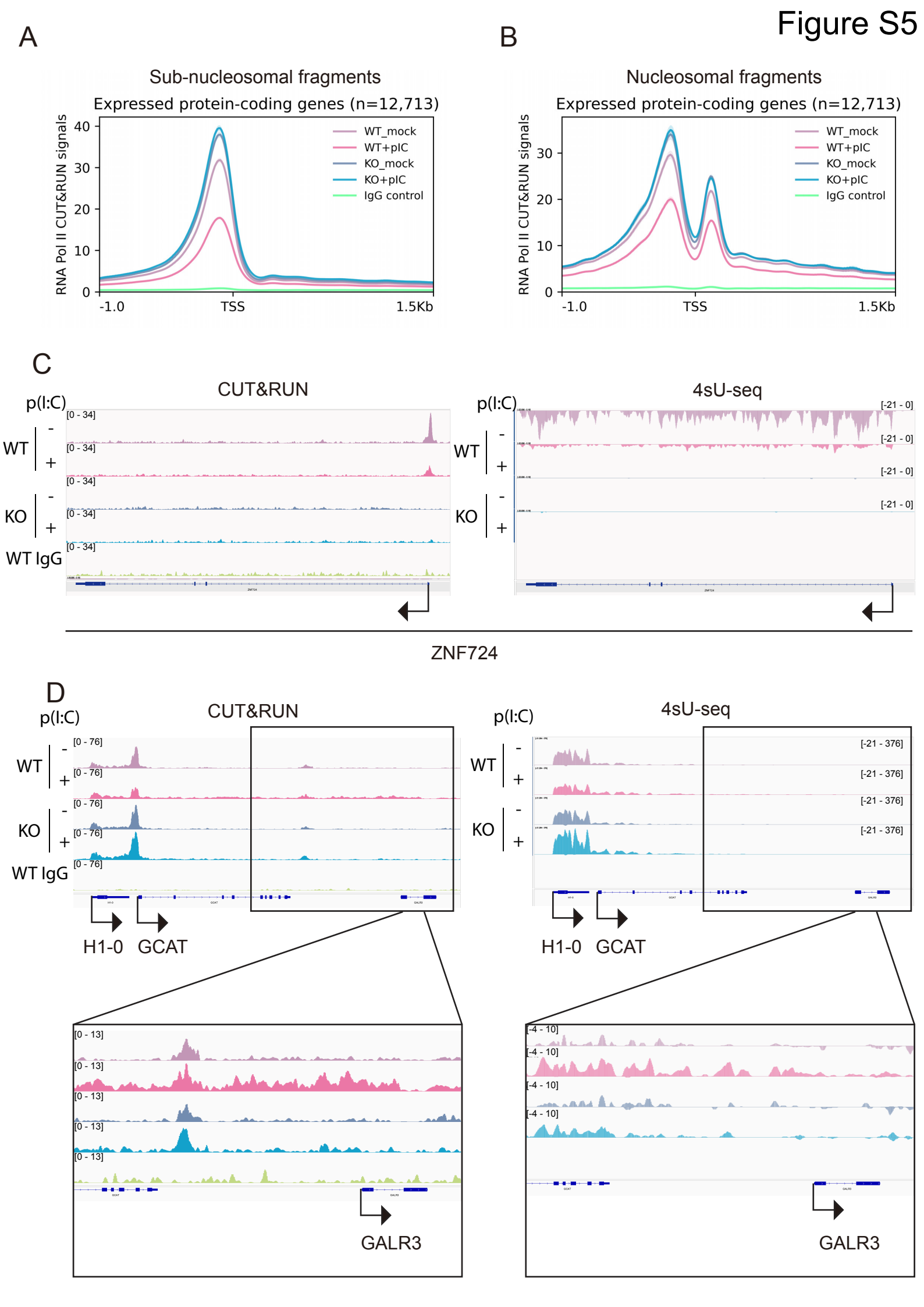
A
Sub-nucleosomal fragments
Expressed protein-coding genes (n=12,713)
RNA Pol II CUT&RUN signals
WT_mock
WT+pIC
KO_mock
KO+pIC
IgG control
-1.0
TSS
1.5Kb
B
Nucleosomal fragments
Expressed protein-coding genes (n=12,713)
C
CUT&RUN
4sU-seq
p(I:C)
WT
KO
WT IgG
ZNF724
D
H1-0
GCAT
GALR3